# Efficient and Selective Dual-Pathway Polyolefin Hydro-Conversion over Unexpectedly Bifunctional M/$TiO_2$-Anatase Catalysts

Linxiao Chen, Julia B. Moreira, Laura C. Meyer, and János Szanyi*

Institute for Integrated Catalysis, Pacific Northwest National Laboratory, Richland, WA 99352, USA

*Corresponding author: janos.szanyi@pnnl.gov

**Abstract**

The huge scale of plastic waste generation and its environmental consequences drive the demands for catalytic plastic upcycling processes. Here, we report efficient polypropylene (PP) hydro-conversion over Ru and Ni supported on a sol-gel anatase $TiO_2$ ($TiO_2$-A-SG). A small number of Brønsted acid sites on $TiO_2$-A-SG enables hydrocracking, improving efficiency, steering the selectivity towards high-valued $C_{4-20}$, and allowing more isomerization, compared to Ru-based monofunctional hydrogenolysis catalysts. The relative contribution of hydrocracking increases with lower hydrogen partial pressure, more branched substrates, and lower Ru loading. Ni/$TiO_2$-A-SG exhibits superior hydrocracking activity and selectivity to Ni on conventional Brønsted-acidic supports, particularly zeolites. Mechanistic studies shows fast isomerization and sequential $\beta$-scissions caused by strong polymer-catalyst interaction and fast cracking with abundant $^3C$. This favors $C_{4-12}$ formation and prevents secondary reactions. This work demonstrated a novel, highly efficient noble-metal-free catalyst for plastic waste upcycling, while advancing the mechanistic understanding of polyolefin hydro-conversion.

**Keywords:** plastic upcycling; anatase titania; polyolefin; hydrocracking; hydrogenolysis

## 1. Introduction

Single-use plastics have been produced on the large scale of ~380 Mt/yr, creating huge amount of non-degradable waste causing severe pollution of our environment [1]. The inefficacy of current approaches for plastic waste processing, such as recycling and incineration [2], lead to the surging pursuit for chemical routes that "upcycle" it into chemicals, closing the carbon cycle and achieving "circular economy" [3]. Among plastics, polyolefins (POs), including polypropylene (PP) and polyethylene (PE), make up > 50% of the total production [2], and are the most challenging to convert because of the chemical inertness of C−C single bonds. Therefore, the upcycling of POs requires either intensive energy input [4-6], or effective catalytic processes.

Recent works from multiple groups demonstrated PO upcycling to small alkanes on metal catalysts under $H_2$ at ≤ 300 °C, without additional carbon source [7-20]. These reactions require lower temperature and are less susceptible to coking than pyrolysis or acid-catalyzed Haag-Dessau cracking [5, 21, 22]. Also, similar reactions of small hydrocarbons have been staples of the oil refining industry, and hence both operation infrastructure and fundamental knowledge partially transferrable to PO substrates exist. Depending on the mechanism of C−C bond cleavage, these reactions follow two distinct pathways [17, 23]: hydrogenolysis, in which C−C bonds are cleaved on the metal [24-27], through dehydrogenated transition states, and hydrocracking, in which C−C bonds are cleaved on Brønsted acid sites (BAS) [28-30], through $\beta$-scissions of carbenium ions. Nonetheless, such distinction is not always made clearly, which can lead to the misunderstanding of the mechanism and the misuse of the terms [17, 31]. The situation is particularly complicated when the catalyst has BAS on the support and a hydrogenolysis-active metal, on which the two pathways could occur simultaneously [17, 21, 28, 32]. The correct identification of the mechanism and the understanding of PO hydro-conversion under such conditions are crucial but lacking.

Meanwhile, the development and understanding of PO hydro-conversion remain at a preliminary stage. Hydrogenolysis catalysts often have high content of expensive, unsustainable noble metals (Ru or Pt) [7-10, 12, 13, 15, 18, 25, 26, 33-35], and tend to excessively produce low-valued $CH_4$. As for hydrocracking, most works also used noble metals, particularly Pt, for the (de)hydrogenation ability of the catalyst [14, 29, 30, 36-40]. The BAS for C−C bond cleavage were often provided by zeolite supports [36-41], but the microporous structure of them could limit the accessibility of the BAS to the bulky polymers, and skews product distribution towards lower-valued gases [42]. Furthermore, compared to small alkanes, POs possess unique interactions with catalyst surfaces and diffusion properties, which could significantly affect their behaviors in the hydro-conversion [9, 25, 43]. Therefore, mechanistic understanding obtained from small-alkane studies is not entirely applicable to PO substrates, and fundamental studies specific to the hydrocracking of POs, especially PP, are very rare [29].

In this work, we investigated the hydro-conversion of POs over metals supported on a sol-gel anatase $TiO_2$ ($TiO_2$-A-SG). We show that the BAS of low population on $TiO_2$-A-SG allow simultaneous hydrocracking and hydrogenolysis on Ru/$TiO_2$-A-SG, leading to its superior activity and selectivity in PP hydro-conversion to monofunctional Ru catalysts. Lower hydrogen partial pressure ($P_{H2}$), more branches in the substrate, and lower Ru content on the catalyst favor hydrocracking over hydrogenolysis. We also show the advantages of $TiO_2$-A-SG over silica-alumina-based supports in PP hydrocracking. Although, similarities exist between PP and small-alkane substrates, the strong PP-catalyst interaction has significant implications on the mechanism and product distribution. This work elucidates the two distinct pathways for PO hydro-conversion on novel bifunctional catalysts, and general rules on how the reaction pathway is determined. It also offers rare mechanistic understanding on PP hydrocracking over a highly efficient catalyst.

## 2. Experimental Section

### *2.1 Chemicals, materials, and catalyst synthesis*

Polypropylene (PP, isotactic, $M_w$ ~250000 g/mol, $M_n$ ~67000), low-density polyethylene (LDPE, $M_w$ ~4000 g/mol, $M_n$ ~1300), squalane (96%), *n*-$C_{16}H_{34}$ (≥ 99%), $Ru(NO)(NO_3)_x(OH)_y$ (x + y = 3, 1.5 wt% in dilute nitric acid), $Pt(NH_3)_4(NO_3)_2$ (99.995% trace metals basis), and ethyl acetate (EtOAc, HPLC grade, ≥ 99.8%) were purchased from Sigma-Aldrich. $Ni(NO_3)_2 \cdot 6H_2O$ (98%) was purchased from Alfa Aesar. Rutile $TiO_2$ and commercial anatase $TiO_2$ were purchased from US Nano (US 3520, 99.9+%, 30 nm, and US 3838, 99.5%, 5 nm, respectively). $Al_2O_3$ (Puralox, SBA-200) and $Nb_2O_5$ (99.95%) were purchased from Condea and Thermo Scientific, respectively. Amorphous $SiO_2$-$Al_2O_3$ (Si : Al = 15) was acquired from Sigma-Aldrich (grade 135). Beta zeolite (Si : Al = 25) was obtained from Zeolyst in $NH_4^+$ form and calcined at 500 ℃ for 4 h to acquire $H^+$ form. SSZ-13 zeolite (Si : Al = 6) was synthesized in-house for a previous work [44]. Sol-gel anatase $TiO_2$ was synthesized by following the procedure described in detail in references [45, 46]. The metal-loaded catalysts were synthesized by wet impregnation of metal precursors in 15 mL $H_2O$. The catalysts were dried under 400 rpm stirring at 130 ℃, and then calcined at 400 ℃ for 4 h (5 ℃/min ramp rate). No further pre-treatment was performed before the reaction. The hydro-thermal treatment of calcined Ni/$TiO_2$-A-SG was performed following the same procedure with the catalyst synthesis, but with no metal cursor added and in a Teflon liner.

### *2.2 Polyolefin hydro-conversion reactions*

Detailed procedures on the catalytic measurements and definitions of the terms can be found in references [9, 24]. In short, the catalyst and polyolefin were mixed in a glass vial then placed into a Parr autoclave reactor of 125 mL. The reactor was purged with $H_2$ 7 times,

pressurized with $H_2$, and then heated to the desired temperature for the reaction. After quenching in an ice bath, the gas was collected at room temperature and analyzed by GC-TCD (Inficon Micro GC Fusion Gas Analyzer with four modules: Rt-Molsieve 5A, Rt-U-Bond, Rt Alumina, and Rxi-1ms). The detector was calibrated with a calibration gas mixture (Gas and Supply) of $N_2$, $H_2$, CO, $CO_2$, methane, ethane, ethylene, propane, propylene, isobutane, *n*-butane, *n*-butene, isopentane, and *n*-pentane. The liquids were collected, and the solid was extracted with EtOAc. The combined solution was analyzed by GC-FID (Agilent 7890A GC, DB-5 column, Agilent 7693 autosampler). Solid residue was weighed after drying.

*2.3 Catalyst characterization*

Ru/$TiO_2$-A-SG was reduced by 30 bar $H_2$ at 260 ℃ for 3 h prior to all characterizations except for $N_2$ physisorption. Detailed procedures for $N_2$ physisorption, powder X-ray diffraction (XRD), scanning transmission electron microscopy (STEM), and X-ray photoemission spectroscopy (XPS) can be found in reference [46]. The pore distribution was acquired from the BET isotherm of $N_2$ physisorption. For STEM, the sample was reduced and transferred into the vacuum chamber immediately, with air exposure of ~5 min. For XPS, the sample was reduced in an *in-situ* side chamber attached to the XPS instrument by 1 atm $H_2$ again for 10 h before the measurement, and then transferred into the analysis chamber without air exposure. Peak fitting was performed with CasaXPS software. Binding energy (BE) was calibrated with the Ti $2p_{2/3}$ peaks at 458.7 eV. XP spectrum in the C 1*s* + Ru 3*d* region was fit with one symmetric "adventitious" C 1*s* peak, a pair of symmetric C 1*s* peaks with identical FWHM and area with the BE of ~288.8 eV and ~285.7 eV for adsorbed carboxylates, and a pair of Ru $3d_{5/2}$ and $3d_{3/2}$ peaks with the peak shape of LF (0.8, 3, 500, 80), identical FWHM, fixed area ratio, and fixed BE shift.

X-ray absorption spectra (XAS) were collected at beamline 4-1 at the Stanford Synchrotron Radiation Lightsource (SSRL). Ru K-edge XAS spectra of the samples were collected in fluorescence geometry using a 100-element Ge monolith (Canberra/Mirion). A Ru foil was scanned simultaneously in transmission geometry as an internal energy standard. The beamline was calibrated to the maximum of the first derivative for the Ru foil. The *in-situ* XAS sample was prepared by pressing and sieving the as-prepared catalyst to particle sizes of 125 to 177 μm (80-120 mesh size). Approximately 50 mg of the sieved catalyst was loaded into a 3 mm OD x 2.6 mm ID quartz capillary (Hilgenberg) forming a packed bed approximately 1 cm long suspended between pieces of quartz wool. The capillary was installed in a custom-built *in-situ* flow cell, described elsewhere [47], that allowed for the gas atmosphere and temperature to be changed as necessary. The measurements were performed at 260 °C under 20 bar $H_2$ (Airgas grade 5.0, heating under $H_2$). EXAFS analysis was performed with Athena and Artemis in the Demeter software package. Scattering paths used in the EXAFS fitting were calculated with FEFF based on the structure of Ru. $S_o^2$ was determined by fitting the EXAFS of Ru foil in the same experiment.

CO-IR experiments were performed in a vacuum chamber with a Bruker Vertex 80 IR spectrometer. The sample pellet was supported on a tungsten grid. The system was baked overnight, and then the sample was annealed in 1 Torr $O_2$ at 400 °C for 30 min. The sample was then cooled down to liquid-$N_2$ temperature, exposed to 0.13 Torr CO after background collection, and CO was then evacuated with continuous spectrum collection. The same sample was treated by 1 Torr $O_2$ at 500 °C for 4 h before another set of measurements was performed.

## 3. Results and discussion

### *3.1 Efficient and selective dual-pathway PP hydro-conversion over Ru/$TiO_2$-A-SG*

Prompted by the excellent performance of low-coverage (< 0.25 $nm^{-2}$) Ru on $CeO_2$ in PO hydrogenolysis [24], we tested 0.07 $nm^{-2}$ Ru on various supports for the reaction ($T$ = 260 °C, $P_{H2}$ = 30 bar, all catalysts herein noted by Ru coverage in $nm^{-2}$). An anatase $TiO_2$ synthesized by a sol-gel method ("$TiO_2$-A-SG") [45] surprisingly stands out. Table 1 shows that compared to Ru/$CeO_2$, the most active and selective catalyst among others (to be reported in a separated manuscript), Ru/$TiO_2$-A-SG (Ru coverage corresponding to 0.09 wt% Ru) converts PP with much higher per-Ru efficiency (344 $g_{PP} \cdot g_{Ru}^{-1} \cdot h^{-1}$, compared to 108 $g_{PP} \cdot g_{Ru}^{-1} \cdot h^{-1}$), significantly lower selectivity towards undesired $CH_4$ ($S_{CH4}$ = 3.2%, compared to 21%), higher selectivity towards desired liquid ($C_{6-40}$) products ($S_{liquid}$ = 78%, compared to 72%), and better isomerization ability (62% isomerized products in $C_{10}$ [24], compared to 40%). Nevertheless, with LDPE as the substrate, Ru/$TiO_2$-A-SG does not exhibit superior performances to Ru/$CeO_2$: the per-Ru efficiency is comparable, but the selectivity is much worse ($S_{CH4}$ = 46%, $S_{liquid}$ = 39%, compared to 15% and 77%, respectively), with the only advantage being yielding more branched products (50% in $C_{12-22}$, compared to 33%).

**Table 1.** Comparing performances of $Ru/TiO_2$-A-SG and $Ru/CeO_2$ in PO hydro-conversion.

| Substrate | Catalyst | Per-Ru rate ($g_{PO} \cdot g_{Ru}^{-1} \cdot h^{-1}$) | $S_{CH4}$ (%) | $S_{liquid}$ (%) | $S_{isomer}$ (PP) or $S_{branched}$ (LDPE) (%) |
|---|---|---|---|---|---|
| PP | $Ru/TiO_2$-A-SG | 344 | 3.2 | 78 | 62 |
| | $Ru/CeO_2$ | 108 | 21 | 72 | 40 |
| LDPE | $Ru/TiO_2$-A-SG | 429 | 46 | 39 | 50 |
| | $Ru/CeO_2$ | 478 | 15 | 77 | 33 |

Reaction condition: 260 °C, 30 bar $H_2$, 1 g PO, 18 h (PP) or 3 h (LDPE), 0.07 Ru/nm$^2$ on the catalyst, PO conversion between 20% and 60%. Isomer selectivity was analyzed with $C_{10}$, and branched selectivity was analyzed with $C_{12\text{-}22}$.

Intrigued by the excellent performance of $Ru/TiO_2$-A-SG in PP hydro-conversion and the discrepancy between results with PP and LDPE, we characterized the sample in detail, after reduction with 30 bar $H_2$ at 260 °C. $TiO_2$-A-SG has the surface area of 77 m$^2$/g (Table S1) and no micropores of $d$ < 1 nm (Figure 1a). XRD (Figure 1b) shows only diffraction peaks from anatase, verifying the phase purity of $TiO_2$ and indicating the absence of large, crystalline Ru particles. The average diameter of Ru particles was estimated as 1.2 ± 0.3 nm from STEM (Figure 1c), and 1.5 nm from the best fitting model of the Ru K-edge EXAFS (Figure 1d) [48]. Previously we showed that the disordered, flat morphology of Ru on < 0.25 $Ru/CeO_2$ leads to high activity and selectivity in PO hydrogenolysis [24]. Nevertheless, by carefully analyzing the EXAFS of $Ru/TiO_2$-A-SG (Table S2 and related discussions), we concluded that Ru was present as well-defined, three-dimensional particles, and thus the excellent performance in PP hydro-conversion is not due to the morphology of Ru. Meanwhile, in the XANES region (Figure 1e), both the white-line intensity and the line shape of $Ru/TiO_2$-A-SG (red) are close to those of Ru foil (brown) rather than $RuO_2$ (cyan), suggesting close-to-metallic Ru sites, in agreement with the Ru $3d_{5/2}$ binding energy of 279.3 eV in XPS (Figure 1f).

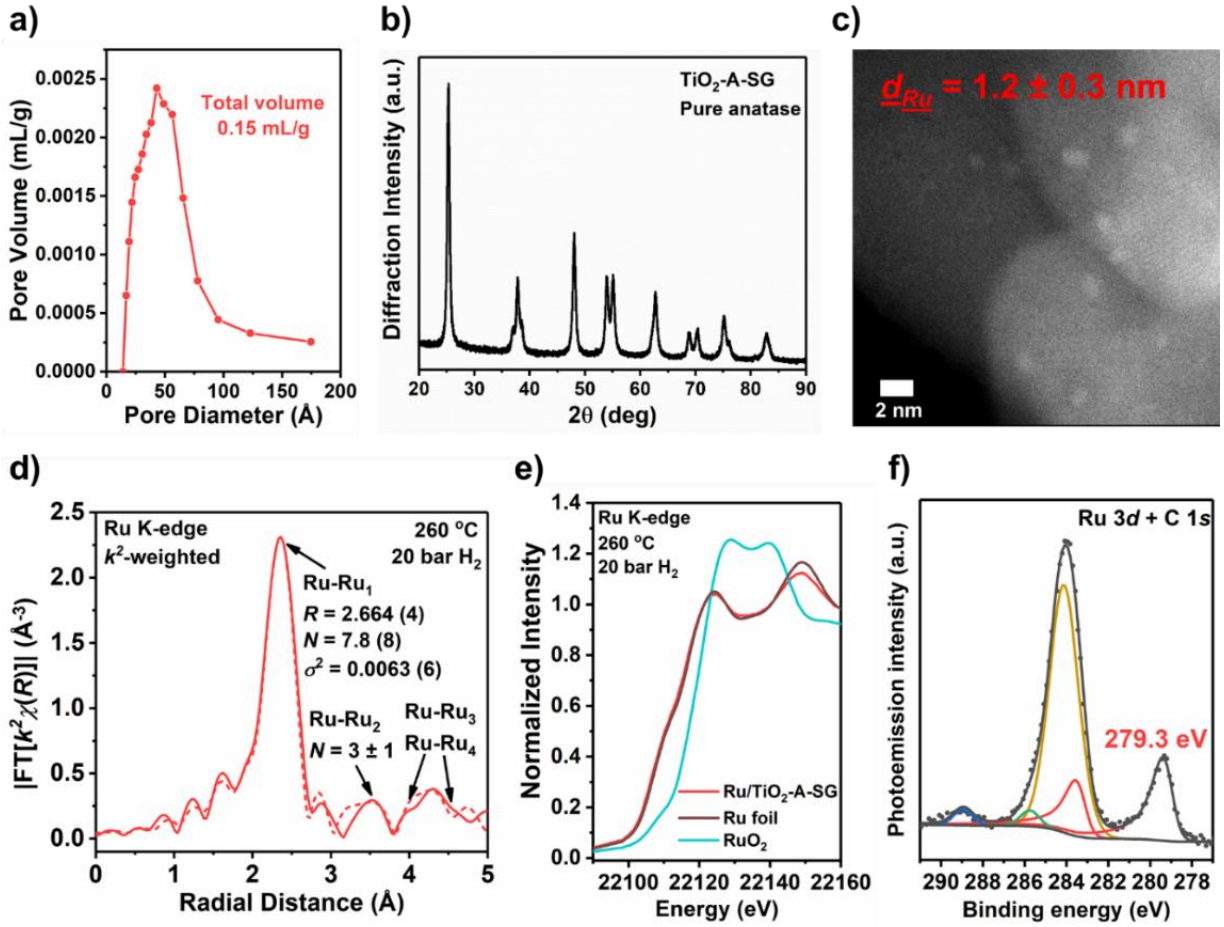


**Figure 1.** Characterization of 0.07 Ru/$TiO_2$-A-SG reduced at 260 °C under 30 bar $H_2$. **a)** Pore size distribution from the BET isotherm. **b)** XRD pattern, which only has anatase-$TiO_2$ peaks. **c)** A representative STEM image. **d)** *R*-space magnitude of $k^2$-weighted Ru K-edge EXAFS, with the best fitting models for data between 1 and 4.8 Å shown as the dashed curves (see Table S2 for fitting parameters). **e)** Normalized XANES spectra, with the spectra of Ru foil and $RuO_2$ shown in brown and cyan, respectively. XAS was collected *in-situ* at 260 °C under 20 bar $H_2$. **f)** XP spectra in the Ru 3*d* + C 1*s* region with fitting, in which red components represent Ru 3*d* peaks, and yellow, blue, and green components represent various forms of C adsorbed from atmosphere. XPS was collected after re-reducing the sample at 260 °C without air exposure.

Detailed analysis of PP hydro-conversion products revealed several distinct characteristics of Ru/$TiO_2$-A-SG, besides the low $S_{CH4}$, high $S_{liquid}$, and high isomerization level. Compared to Ru/$CeO_2$ (Figure 2a), which is representative of other Ru catalysts, Ru/$TiO_2$-A-SG (Figure 2b) yields minimal $C_{2\text{-}3}$, abundant $C_{4\text{-}5}$, and a narrow liquid product distribution around $C_{10}$ rather than a wide distribution around $C_{22}$. Also, both the liquid and the solid residue are of light yellow color

(Figures S1a-b), rather than colorless products formed on $Ru/CeO_2$ [24], implying the presence of low-concentration of unsaturated hydrocarbons. Since the simultaneously occurring isomerization and the lack of $C_{1-2}$ are characteristic of $\beta$-scissions through carbenium ions ($C^+$) [21, 29, 30, 42, 49-51], we tested 0.07 Ni and $Pt/TiO_2$-A-SG (coverage corresponding with 0.055 wt% Ni and 0.18 wt% Pt), which are inactive for hydrogenolysis under identical conditions [9, 24, 25]. Figure 2d shows that both Ni and $Pt/TiO_2$-A-SG convert PP faster than $Ru/TiO_2$-A-SG, with similar product distribution characteristics (Figures 2c and S2a): trace $C_{1-2}$, minimal $C_3$, abundant $C_{4-5}$, high selectivity towards liquid products with a narrow distribution around ~$C_{10}$ and high isomerization level. Since neither Ni nor Pt catalyzes C−C bond cleavage under the testing conditions applied here, the results indicate that the C−C bond cleavage occurs on $TiO_2$-A-SG support . This aligns with the commonly accepted hydrocracking mechanism (red in Scheme 1) [21], in which C−C bonds are cleaved on BAS, typically on the support, while the metal only catalyzes the dehydrogenation of the alkane substrate and the re-hydrogenation of the products. In fact, PP can also be converted slowly on $TiO_2$-A-SG without any metals (Figure 2d), which is significantly facilitated by physically mixing in a (de)hydrogenation catalyst (5% $Ni/Al_2O_3$), and yields similar product distribution with Ni and $Pt/TiO_2$-A-SG (Figures S2b-c). These results suggest that $Ru/TiO_2$-A-SG also converts PP through hydrocracking, which explains its superior performance to and drastically different behaviors from $Ru/CeO_2$. We note that when the metal component on $TiO_2$-A-SG is not Ru, $C_{1-2}$ yields are always minimal, suggesting that the C−C bond cleavage follows $\beta$-scissions rather than protolytic (Haag-Dessau) cracking mechanism, which usually operates at higher temperature [21, 52-54]. Since $\beta$-scissions of branched substrates (PP) strongly favors *i*-$C_4$ over $C_{2-3}$ [21], we will use the ratio between $C_{2-3}$ yields and *i*-$C_4$ yield ( "($C_2$ + $C_3$) / $C_4$", cyan dots in Figures 2d and below) as a reaction pathway indicator, along with $S_{CH4}$ (green

dots in Figures 2d and below). PO hydrogenolysis on our monofunctional Ru catalysts without hydrocracking always yields $(C_2 + C_3) / C_4 > 2.0$ (Figure S3) and $S_{CH4} > 10\%$ [9, 24].

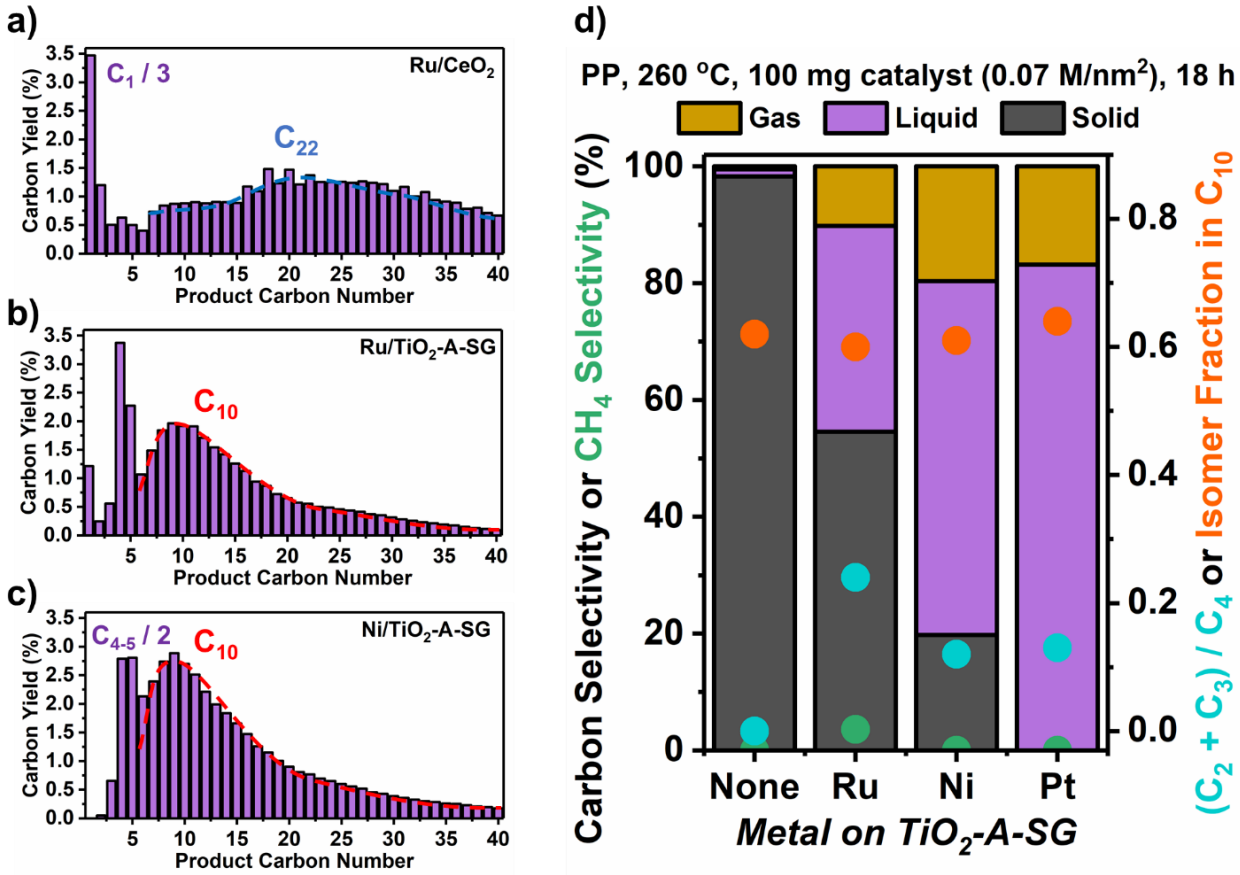


**Figure 2. a)** – **c)** Carbon yields of $C_{1\text{-}40}$ products from PP hydro-conversion over 0.07 $Ru/CeO_2$, 0.07 $Ru/TiO_2$-A-SG, and 0.07 $Ni/TiO_2$-A-SG, repsectively. In **a)**, $C_1$ yield is plotted with 1/3 of its original value. In **c)**, $C_{4\text{-}5}$ yields are plotted with half of their original values. Reaction conditions can be found in [24] and panel d), with PP conversion between 50% and 80%. **d)** The performance of 0.07 $nm^{-2}$ Ru, Pt, or Ni on $TiO_2$-A-SG in PP hydro-conversion under 30 bar $H_2$. Black, purple, and yellow bars represent carbon selectivity in solid, liquid, and gas phases after the reaction (left *y*-axis). Green dots represent $S_{CH4}$ (left *y*-axis). Cyan dots represent the $(C_2 + C_3) / C_4$ value, i.e., the ratio between $C_{2\text{-}3}$ yields, and *i*-$C_4$ yield (right *y*-axis). Orange dots represent the fraction of isomerized products in all $C_{10}$ products. Reactions on Ni and $Pt/TiO_2$-A-SG at lower conversions (see Figures 7 and S7a below) show similar selectivity with the high-conversion reactions reported in this figure.

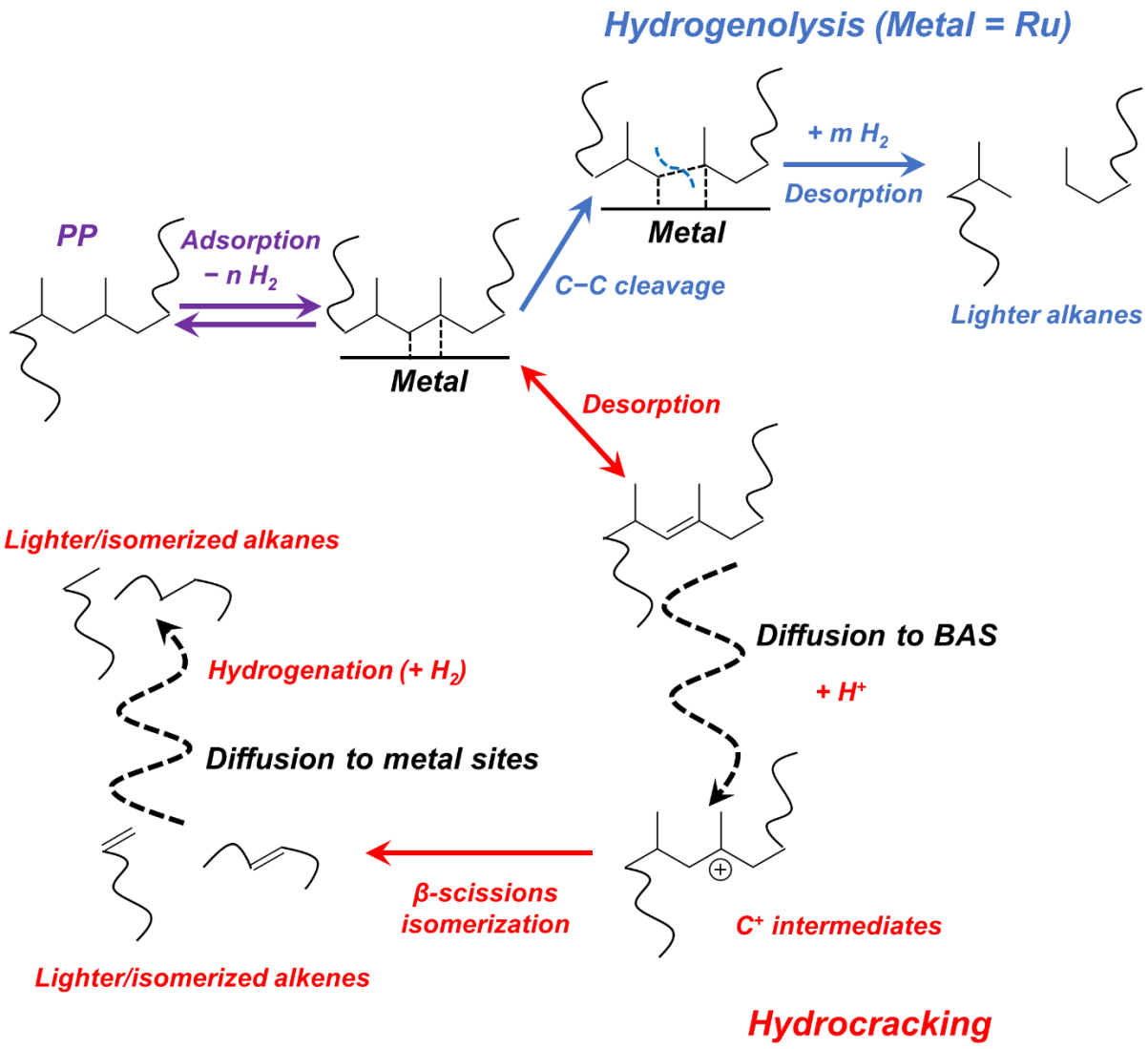


**Scheme 1.** Schematic of the two PP hydro-conversion pathways that occur simultaneously on Ru/$TiO_2$-A-SG at 260 °C. In hydrogenolysis, C−C bonds are cleaved on Ru sites, while in hydrocracking, C−C bonds are cleaved on the Brønsted acid sites on $TiO_2$-A-SG.

*3.2 Brønsted-acid hydrocracking active sites on $TiO_2$-A-SG revealed by IR spectra of adsorbed CO*

The ability of M/$TiO_2$-A-SG to catalyze PP hydrocracking was a surprise, as XPS shows no contamination on the surface of $TiO_2$-A-SG (Figure S4), and pure anatase $TiO_2$ is not usually

known as active in BAS-catalyzed reactions such as alkane hydrocracking [55-57]. Thus, we used IR experiments with probe molecules to examine the surface acidity of Ni/$TiO_2$-A-SG. The red curves in Figures 3a-b show the IR difference spectra after adsorbing CO onto fresh Ni/$TiO_2$-A-SG at liquid-$N_2$ temperature followed by evacuation, in the $\nu$(O−H) and $\nu$(C=O) regions, respectively. The adsorption of CO leads to a set of negative $\nu$(O−H) bands at 3637, 3667, 3685, 3718, and 3745 $cm^{-1}$, along with a wide positive $\nu$(O−H) band between 3400 and 3600 $cm^{-1}$, corresponding with the interaction between surface ─OH and CO to form H-bonds [58-60]. The H-bonded CO species ($CO_{H\text{-}bond}$) produces $\nu$(C=O) bands at 2153 and 2165 $cm^{-1}$, in addition to the intense bands at 2210 and 2180 $cm^{-1}$ from CO adsorbed on $\alpha$- and $\beta$-types of $Ti^{4+}$ Lewis-acid sites (LAS, $CO_{\alpha\text{-}Ti}$ and $CO_{\beta\text{-}Ti}$), respectively. The weak bands at ~2135 $cm^{-1}$ was assigned to physisorbed CO ($CO_{phy}$) [58-60]. During subsequent evacuation, the intensities of $\nu$(O−H) and $\nu$(C=O) bands associated with $CO_{H\text{-}bond}$ decrease simultaneously (Figures S5a-b), confirming that they are from the same species, and suggesting that the formation of H-bonds between surface ─OH and CO is partially reversible. The fact that the intensities of these bands are partially retained after prolonged evacuation indicates that some of the surface OH groups possess high enough Bronsted acidity to hold onto CO molecules even under high vacuum. Meanwhile, the adsorption of pyridine onto fresh Ni/$TiO_2$-A-SG at 150 ℃ leads to bands at 1643 and 1543 $cm^{-1}$, assigned to the 8a and 19b vibration modes of pyridine ions protonated on BAS ("B-py", Figure S5c), respectively [61, 62]. The ability of the surface ─OH on Ni/$TiO_2$-A-SG to form H-bonds with CO and protonate pyridine indicates their Brønsted acidity.

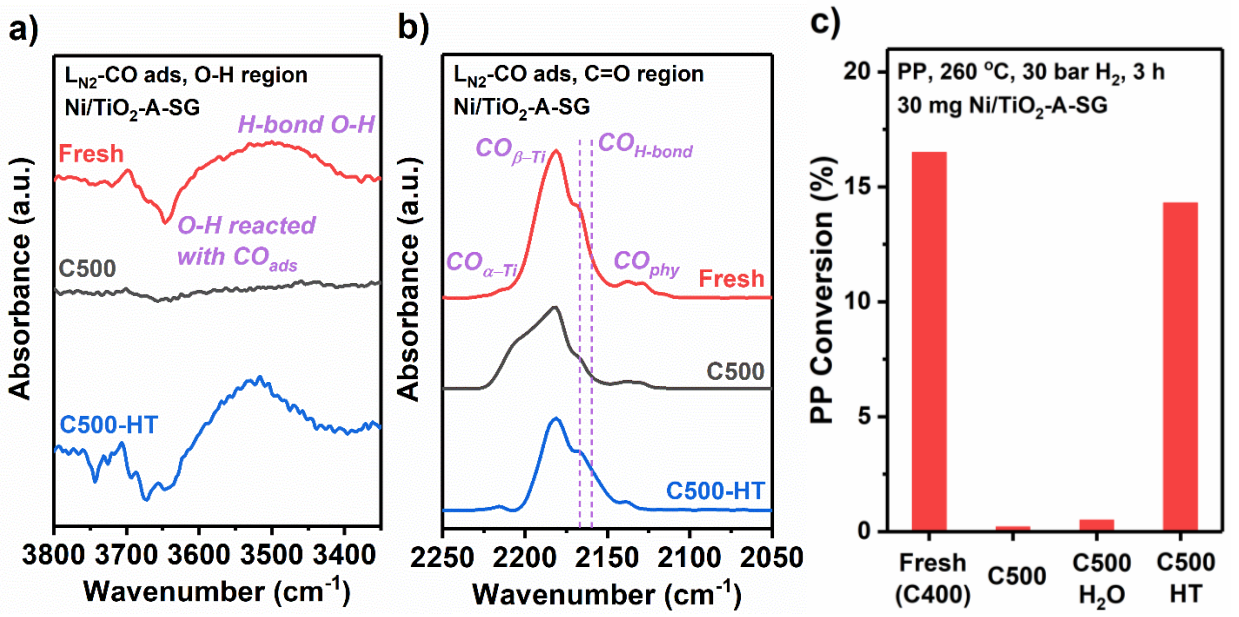


**Figure 3.** CO-IR experiments showing the Brønsted acidity of Ni/$TiO_2$-A-SG and its correlation with hydrocracking activity. **a)** – **b)** Differential spectra after exposing the sample to 0.13 Torr CO at liquid-$N_2$ temperature followed by complete evacuation, in the $\nu$(O–H) and $\nu$(C=O) regions, respectively. Red, black, and blue curves show data on the sample in its fresh form ("fresh"), after calcination at 500 °C for 4 h in static air ("C500"), and after C500 then hydro-thermal treatment at 130 °C in a Teflon liner ("C500-HT"). Spectra during CO evacuation on the fresh sample can be found as Figures S5a-b. **c)** PP conversion on the sample after various treatments under identical conditions. The experiments were performed with 1.3 $nm^{-2}$ Ni.

In Figure 3b, the intensity of the $CO_{H\text{-}bond}$ bands is much lower than that of $CO_{\alpha\text{-}Ti}$ and $CO_{\beta\text{-}Ti}$ bands, and in Figure S5c, the intensity of B-py bands is much lower than that of bands at 1611 and 1449 $cm^{-1}$, which are associated with the 8a and 19b vibration modes of pyridine adsorbed on LAS ("L-py"), respectively [61, 62]. These observations suggest that the population of BAS on Ni/$TiO_2$-A-SG is significantly lower than that of LAS, as agreed in the literature on anatase [55-57]. Therefore, we questioned whether PP hydrocracking is actually catalyzed by the BAS. We noticed that calcining Ni/$TiO_2$-A-SG at 500 °C ("C500" in Figure 3c) eliminates its activity in PP hydrocracking. Since $TiO_2$-A-SG was calcined at 500 °C prior to Ni impregnation, the stirring of $TiO_2$-A-SG in water at 130 °C had to generate the active site for hydrocracking. Indeed, Figure 3c

shows that the hydrocracking activity of C500 Ni/$TiO_2$-A-SG can be recovered by a hydro-thermal treatment at 130 ℃ ("C500-HT"), but not by water adsorption at room temperature ("C500-$H_2O$", see reference [63] for the procedure). Meanwhile, Figures 3a-b show that C500 Ni/$TiO_2$-A-SG does not have surface ─OH that can form H-bonds with CO (black, differential spectra before and after the 500 ℃ calcination in Figure S5d showing the loss of ─OH), which are replenished after the hydro-thermal treatment (blue). In contrast, the 500 ℃ calcination does not alter the overall intensity of CO-on-LAS bands significantly, only converting some $\beta$-Ti sites into $\alpha$-Ti sites. The elimination and recovery of hydrocracking activity by the 500 ℃ calcination and the subsequent hydro-thermal treatment coincide with the removal and replenishment of Brønsted-acidic −OH groups, strongly indicating that the BAS are indeed the active sites for PP hydrocracking, despite their low population. To our knowledge, the catalytic activity of BAS on anatase $TiO_2$ has seldom been recognized, and hence these results could have significant general implications in acid-catalysis beyond PP hydrocracking.

*3.3 Effects of $P_{H2}$, substrate, and Ru loading on the pathway of PO hydro-conversion*

In Figure 2d, $S_{CH4}$ and ($C_2$ + $C_3$) / $C_4$ are both slightly higher on Ru/$TiO_2$-A-SG (3.2% and 0.24) than on Ni and Pt/$TiO_2$-A-SG (0% and ~0.16), indicating that hydrogenolysis also occurs on Ru, to a minor extent. The dual-pathway PP conversion on Ru/$TiO_2$-A-SG was examined under various $P_{H2}$. Figure 4a shows that at $P_{H2} \leq 30$ bar, $S_{CH4}$ remains < 5%, and ($C_2$ + $C_3$) / $C_4$ remains < 0.3. Both values increase abruptly at $P_{H2}$ = 45 bar, to 20% and 1.0, respectively. In PO hydrogenolysis, high $P_{H2}$ reduces $S_{CH4}$ by 1) favoring internal over external C−C bonds in the first C−C bond cleavage [9, 24], and 2) facilitating the hydrogenative desorption of *$C_xH_y$ after the first C−C bond cleavage, thus suppressing sequential cleavages that tend to produce $CH_4$ [64]. ($C_2$ + $C_3$) / $C_4$ also always decreases with increasing $P_{H2}$ (Figure S3). Thus, the increase in both values

at $P_{H2} \geq 45$ bar cannot be explained by selectivity shifts in hydrogenolysis. Meanwhile, the liquid products shift from a narrow distribution around ~$C_{12}$ with yellow color at $P_{H2} \leq 30$ bar (Figures S2f-h, S1a, and S1c), to a wide double distribution around ~$C_{12}$ and ~$C_{18}$ with no color at $P_{H2} \geq 45$ bar (Figures S2i-j and S1d-e). These observations suggest that at low $P_{H2}$ ($\leq$ 30 bar), hydrocracking is the prevailing pathway, while hydrogenolysis becomes significant at $P_{H2} \geq 45$ bar. We note that in the high-$P_{H2}$ regime, the isomerization level remains high (~63%), which, along with the double distribution of liquid products, indicates non-negligible contribution from hydrocracking. The higher relative contribution of hydrogenolysis at higher $P_{H2}$ suggests that its rate is more dependent on $P_{H2}$ than that of hydrocracking, which can be rationalized as that $H_2$ directly assists the C–C bond cleavage in hydrogenolysis but not hydrocracking.

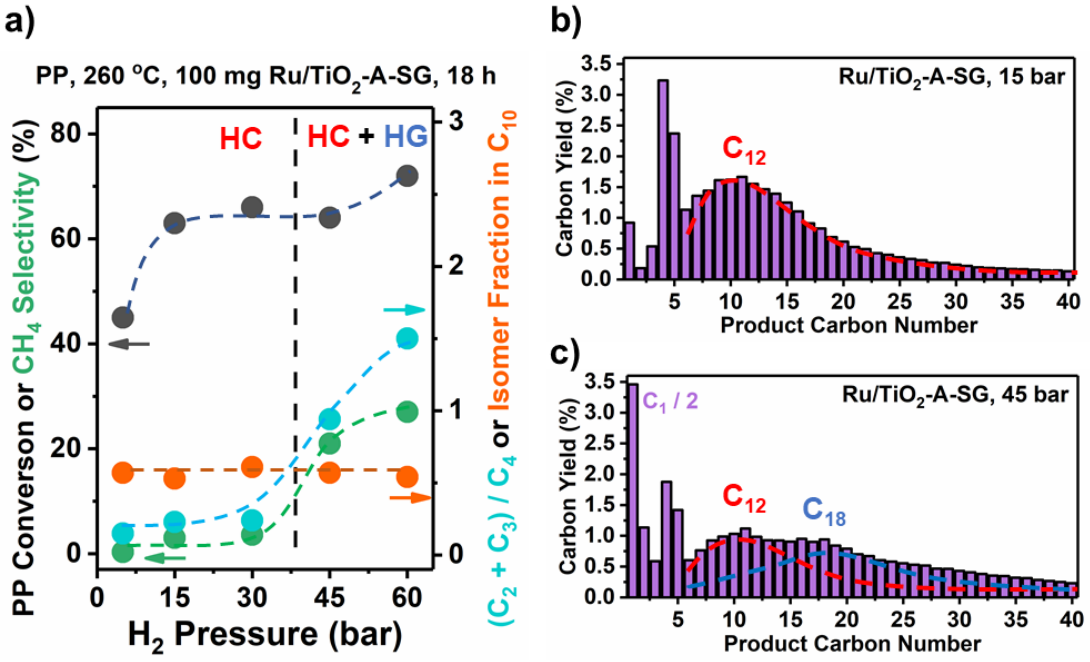


**Figure 4.** Effects of $P_{H2}$ on PP hydro-conversion over Ru/$TiO_2$-A-SG. **a)** Variations in the PP conversion (black, left *y*-axis), $S_{CH4}$ (green, left *y*-axis), ($C_2$ + $C_3$) / $C_4$ (cyan, right *y*-axis), and the fraction of isomerized products in $C_{10}$ (orange, right *y*-axis) with $P_{H2}$. **b)** – **c)** Representative examples of product distribution in the low- ($\leq$ 30 bar) and high-$P_{H2}$ ($\geq$ 45 bar) regime, respectively (see Figures S2f-j for complete data). [HC: hydrocracking; HG: hydrogenolysis]

We also tested the reaction of some other alkanes with varying branching levels ( *n*-$C_{16}H_{34}$, no $^{3}C$; LDPE, ~ 2% $^{3}C$ in total C [65], squalane, structure see Scheme S1a, 20% $^{3}C$, and PP, 33% $^{3}C$) on Ru/$TiO_2$-A-SG, at $P_{H2}$ = 5 and 30 bar. Each substrate was also tested on Ni/$TiO_2$-A-SG at $P_{H2}$ = 30 bar. Since hydrogenolysis does not occur on Ni, and its rate is more sensitive to $P_{H2}$ than that of hydrocracking, we calculated the ratio between the conversion rates 1) on Ni and Ru at $P_{H2}$ = 30 bar, and 2) at $P_{H2}$ = 5 and 30 bar on Ru, to gauge the relative importance of the two pathways. Table 2 shows that as substrate branching level increases, both ratios increase, i.e., the relative contribution of hydrocracking to the overall reaction increases. The conclusion is further supported by that on Ru/$TiO_2$-A-SG, highly branched squalane and PP always yield lower ($C_2$ + $C_3$) / $C_4$ than sparsely branched LDPE and *n*-$C_{16}H_{34}$ under identical conditions (Table 2). It can be explained by the understanding of small-alkane hydro-conversion in the literature, that 1) in hydrocracking, the rate of $\beta$-scissions increases drastically as the branching level of $C^+$ intermediates increases [21], and 2) in hydrogenolysis, the cleavage of $^{3}C–^{x}C$ bonds is slower than that of $^{2}C–^{2}C$ and $^{2}C–^{1}C$ bonds due to the high steric hindrance [66, 67].

**Table 2.** The hydro-conversion of alkanes of various branching levels over M/$TiO_2$-A-SG.

| Substrate ($^3$C frac.) | Metal | $P_{H2}$ (bar) | Conv. (%) | $r$(Ni) : $r$(Ru) at 30 bar | $r$(5 bar) : $r$(30 bar) on Ru | $S_{CH4}$ (%) | ($C_2$ + $C_3$) / $C_4$ |
|---|---|---|---|---|---|---|---|
| *n*-$C_{16}H_{34}$ (0) | Ni | 30 | 0.7 | 0.05 | 0.18 | 0 | 0.1 |
| | Ru | 30 | 14 | | | 23 | 2.9 |
| | | 5 | 2.6 | | | 15 | 2.1 |
| LDPE (~0.02) | Ni | 30 | 7.0 | 0.28 | 0.18 | 0 | 0 |
| | Ru | 30 | 25 | | | 45 | 4.7 |
| | | 5 | 4.5 | | | 30 | 2.0 |
| Squalane (0.2) | Ni | 30 | 7.4 | 0.65 | 0.48 | 0 | 0 |
| | Ru | 30 | 11 | | | 8.0 | 2.6 |
| | | 5 | 5.4 | | | 3.0 | 1.0 |
| PP (0.33) | Ni | 30 | 88 | 1.44 | 0.60 | 0 | 0 |
| | Ru | 30 | 59 | | | 3.2 | 0.24 |
| | | 5 | 37 | | | 0.3 | 0.15 |

Reaction condition: 260 °C, 1 g substrate, *m*(catalyst) and reaction time as following: *n*-$C_{16}H_{34}$ – 8 mg, 3 h; LDPE – 50 mg, 3 h; squalane – 8 mg, 3 h; PP – 100 mg, 18 h.

The reactions of sparsely branched LDPE and *n*-$C_{16}H_{34}$ on Ru/$TiO_2$-A-SG were performed over the entire $P_{H2}$ range for further understanding. Figures 5a-b show that with both substrates, at $P_{H2} \geq 15$ bar, as $P_{H2}$ increases, the conversion (black dots, left *y*-axis) increases first then decreases, while both $S_{CH4}$ and branched alkane fraction from LDPE (red dots, right *y*-axis in Figure 5a) decrease monotonously. These behaviors are typical for alkane hydrogenolysis, as results of the increasing *H coverage on Ru with increasing $P_{H2}$ [9, 24]. In addition, ($C_2$ + $C_3$) / $C_4$ decreases monotonously with increasing $P_{H2}$, also matching previous observations in PO hydrogenolysis (Figure S3) [9, 24]. In contrast, at $P_{H2}$ = 5 bar, characteristics associated with hydrocracking, i.e., low $S_{CH4}$, low ($C_2$ + $C_3$) / $C_4$, and high isomerization level (gauged by the fraction of branched products from *n*-$C_{16}H_{34}$, Figure 5b), emerge. These results suggest that with the sparsely branched alkane substrates, hydrogenolysis is the prevailing pathway at $P_{H2} \geq 15$ bar, and hydrocracking

only becomes important at the low $P_{H2}$ of 5 bar. Even at $P_{H2}$ = 5 bar, both $S_{CH4}$ and ($C_2$ + $C_3$) / $C_4$ on Ru/$TiO_2$-A-SG are much higher than those on Ni/$TiO_2$-A-SG in Table 2, suggesting that the contribution from hydrogenolysis is not negligible. This is in sharp contrast to the highly branched PP, which mainly goes through hydrocracking at $P_{H2} \leq 30$ bar (Figure 4). The results explain why in Table 1, the bifunctional Ru/$TiO_2$-A-SG exhibits worse performance than the monofunctional Ru/$CeO_2$ in LDPE hydro-conversion – the contribution of hydrocracking is minimal, while the well-defined, three-dimensional Ru particles on $TiO_2$-A-SG is less selective in hydrogenolysis than the disordered, flat Ru rafts on $CeO_2$ [24].

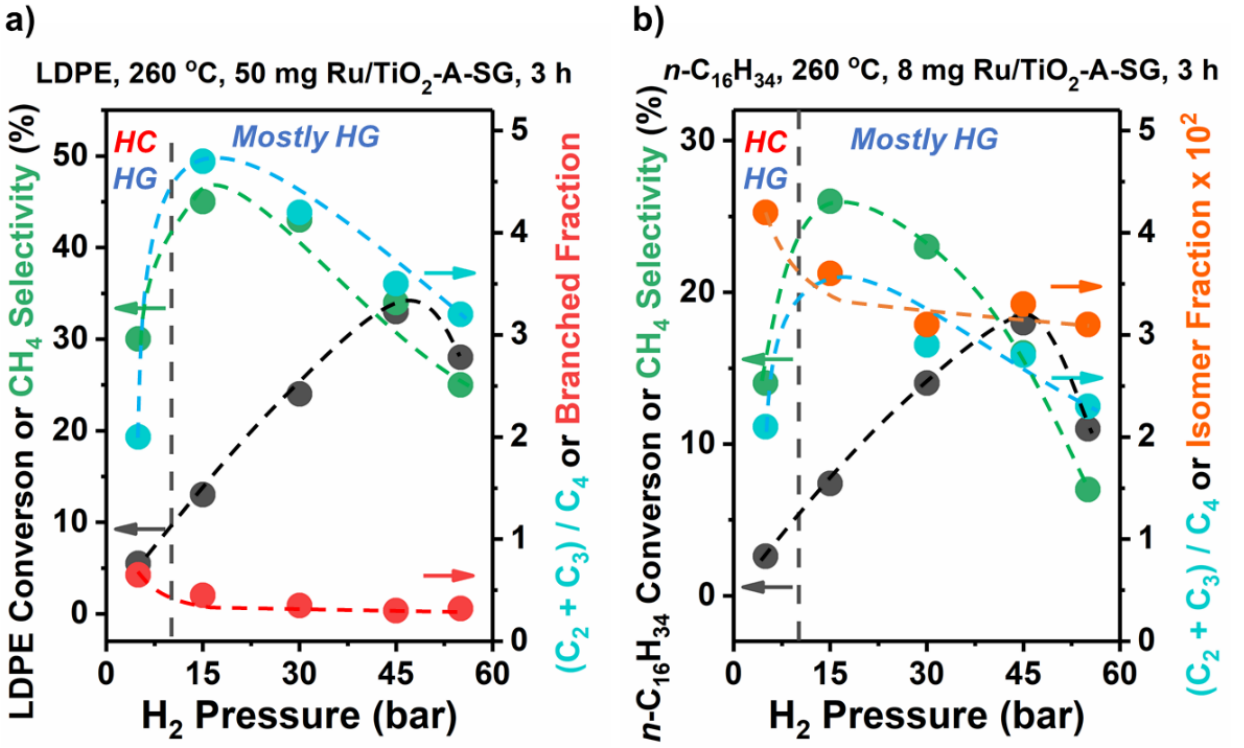


**Figure 5.** Effects of $P_{H2}$ on the hydro-conversion of sparsely branched alkanes, **a)** LDPE and **b)** *n*-$C_{16}H_{34}$, over Ru/$TiO_2$-A-SG. Black, green, and cyan dots show the substrate conversion (left *y*-axis), $S_{CH4}$ (left *y*-axis), and ($C_2$ + $C_3$) / $C_4$ (right *y*-axis), respectively. Red dots in panel a) represent the fraction of branched products from LDPE, while orange dots in panel b) represent the fraction of branched alkanes, i.e., isomers, from *n*-$C_{16}H_{34}$. [HC: hydrocracking; HG: hydrogenolysis]

The $C_{10}$ products from squalane were analyzed in detail for further mechanistic insights. Table 3 shows that on Ru/$TiO_2$-A-SG at $P_{H2}$ = 30 bar, 75% of the $C_{10}$ products are not isomerized (see Figure S6 and related discussions for details of the analysis), indicating that hydrogenolysis is the main reaction pathway. Meanwhile, under such conditions, the absolute majority of non-isomerized products are dimethyloctanes, which are produced from squalane by cleaving exclusively $^{2}C–^{2}C$ bonds (blue in Scheme S1b), rather than methylnonanes, the formation of which requires cleaving at least one $^{3}C–^{x}C$ bond (red in Scheme S1b). The dominance of dimethyloctane without significant isomerization indicates that in hydrogenolysis, the cleavage of $^{2}C–^{2}C$ bonds is strongly favored over that of $^{3}C–^{x}C$ bonds, aligning well with the literature of small-alkane hydrogenolysis [66, 67]. In comparison, at $P_{H2}$ = 5 bar or on Ni/$TiO_2$-A-SG, $C_{10}$ products are much more isomerized, further supporting that decreasing $P_{H2}$ or replacing Ru with the hydrogenolysis-inactive Ni steers the reaction pathway from hydrogenolysis to hydrocracking.

**Table 3.** Distribution of $C_{10}$ products from squalane hydro-conversion over M/$TiO_2$-A-SG.

| Metal, $P_{H2}$ [a] | Non-isomer fraction [b] | Dimethyloctanes : Methylnonanes |
|---|---|---|
| Ru, 30 bar | 75% | 49 |
| Ru, 5 bar | 34% | 25 |
| Ni, 30 bar | 10% | N/A |

[a] Reaction conditions are identical with Table 2.
[b] "Non-isomers" include dimethyloctanes and methylnonanes.

Finally, we evaluated the effects of Ru loading in Ru/$TiO_2$-A-SG on the pathway of PP hydro-conversion. Table 4 shows that at $P_{H2}$ = 30 bar, compared to 0.07 Ru/$TiO_2$-A-SG, 0.14 Ru/$TiO_2$-A-SG exhibits significantly higher $S_{CH4}$ (54.5% compared to 3.2%), ($C_2$ + $C_3$) / $C_4$ (3.4 compared to 0.24), and lower isomerization level (25% in $C_{10}$ compared to 62%), indicating much higher relative contribution of hydrogenolysis. The hydrocracking characteristics become

prominent as $P_{H2}$ decreases to 5 bar, but both $S_{CH4}$ and $(C_2 + C_3) / C_4$ are still higher than those on 0.07 Ru/$TiO_2$-A-SG under the same conditions (7.5% and 0.30, compared to 0.3% and 0.18, respectively). Under both conditions, liquid products on 0.14 Ru/$TiO_2$-A-SG clearly exhibit the $C_{11} – C_{20}$ double distribution (Figures S2d-e) characteristic of simultaneous hydrocracking and hydrogenolysis, in contrast to the narrow single distribution around $C_{11}$ on 0.07 Ru/$TiO_2$-A-SG (Figures S2f and S2h). These results indicate that increasing Ru loading increases the tendency of the reaction to occur through hydrogenolysis. This is expected with the increased ratio between Ru, the active sites for C−C bond cleavage in hydrogenolysis, and the BAS, the active sites for C−C bond cleavage in hydrocracking, as well as the well-established positive dependence of hydrogenolysis TOF on Ru particle size [68, 69].

**Table 4.** Effects of Ru loadings on the PP hydro-conversion over Ru/$TiO_2$-A-SG.

| $P_{H2}$ | Ru coverage ($nm^{-2}$) | PP conversion (%) | $S_{CH4}$ (%) | $(C_2 + C_3) / C_4$ | Isomer fraction (%) |
|---|---|---|---|---|---|
| 30 | 0.14 | 39 | 54.5 | 3.4 | 25 |
| | 0.07 | 59 | 3.2 | 0.24 | 62 |
| 5 | 0.14 | 36 | 7.5 | 0.30 | 60 |
| | 0.07 | 37 | 0.3 | 0.18 | 65 |

Reaction conditions: 260 °C, 18 h, 1 g PP, 100 mg catalyst.

*3.4 Superior PP hydrocracking performance of $TiO_2$-A-SG to other Brønsted-acidic supports*

Results above show that the noble-metal-free 0.07 Ni/$TiO_2$-A-SG efficiently converts PP through hydrocracking. We compared its performance with 0.07 $nm^{-2}$ Ni (calculated based on total surface area, corresponding Ni wt% shown in Table 1) on several conventional Brønsted-acidic supports. Figure 6 shows that amorphous $SiO_2$-$Al_2O_3$ (Si : Al = 15), Beta zeolites (Si : Al = 25), SSZ-13 zeolites (Si : Al = 6), and $Nb_2O_5$ [11, 70, 71] all convert PP at slower rates (red dots, right

*y*-axis) than $TiO_2$-A-SG under identical conditions. Among silica-alumina-based supports, the small-pore SSZ-13 ($d \approx 0.37$ nm), despite its lower Si : Al ratio, exhibits lower PP conversion than the larger-pore Beta ($d \approx 0.65$ nm) and amorphous $SiO_2$-$Al_2O_3$ (30% compared to 51% and 55%). This is likely due to the small pores limiting the accessibility of BAS to the bulky polymers, and the diffusion of polymeric alkenes between Ni and BAS (Scheme 1). Even with 10 times Ni coverage and surface area (Table S1), SSZ-13 is still less effective than $TiO_2$-A-SG (54% PP conversion on "0.7 SSZ-13", compared to 90%), highlighting the advantages of the non-microporous structure of $TiO_2$-A-SG. We also tested a commercial anatase $TiO_2$ ("$TiO_2$-A-C"), which shows much lower rate than $TiO_2$-A-SG. The superior activity of $TiO_2$-A-SG to the non-microporous $SiO_2$-$Al_2O_3$, $TiO_2$-A-C, and $Nb_2O_5$ is currently under further investigation, and hypothesized to be related to the location and accessibility of the BAS.

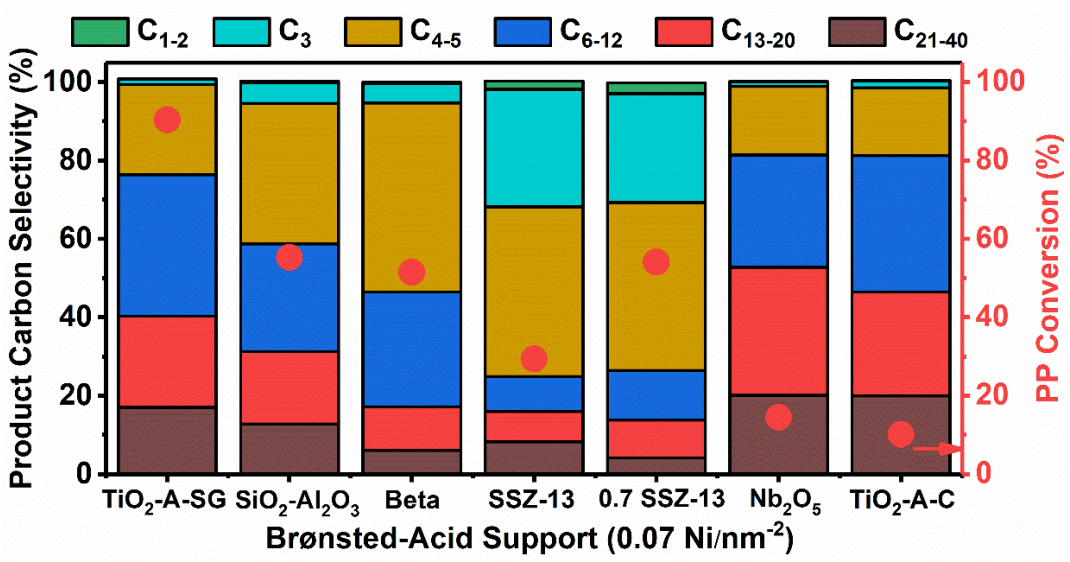


**Figure 6.** Comparing the performance of various Brønsted-acidic supports loaded with 0.07 $nm^{-2}$ Ni in PP hydrocracking. Red dots represent the PP conversion (right *y*-axis), while stacked green, cyan, yellow, blue, red, and brown bars represent the carbon selectivity towrads $C_{1\text{-}2}$, $C_3$, $C_{4\text{-}5}$, $C_{6\text{-}12}$, $C_{13\text{-}20}$, and $C_{21\text{-}40}$ products. "$TiO_2$-A-C" is a commercial anatase, and "$SiO_2$-$Al_2O_3$" is an amorphous $SiO_2$-$Al_2O_3$. The "0.7 SSZ-13" sample have 0.7 $nm^{-2}$ Ni instead of 0.07 $nm^{-2}$ on it. $SiO_2$-$Al_2O_3$, Beta and SSZ-13 zeolites have the Si : Al ratio of 15, 25 and 6, repsectively. Reaction conditions: 260 °C, 30 bar $H_2$, 18 h, 1 g PP, 100 mg catalyst.

Meanwhile, Figures 6 and 2c show that PP hydrocracking on 0.07 Ni/$TiO_2$-A-SG strongly favors light $C_{4-12}$ products in the gasoline range, particularly $C_{4-5}$ (~20% selectivity, yellow bars). In hydrocracking, the high selectivity towards $C_{4-6}$ ($C_6$ underestimated due to volatility) reflects extensive sequential $\beta$-scissions dominated by type-A $\beta$-scissions (ones involving two $^3C^+$ intermediates, Scheme 2). This scenario means that after one $\beta$-scission, the cracked $C^+$ fragment left on the BAS cannot be timely displaced by free alkenes before the next $\beta$-scission occurs (illustrated in Scheme 2), so that it continues to crack unless being too small for $\beta$-scissions ($< C_7$) [21, 29, 51]. We note that, as we will show in section 3.5, the selectivity of hydrocracking is insensitive to PP conversion at < 100%, and hence can be fairly compared among the samples despite different PP conversions. Figure 6 shows that all silica-alumina-based supports exhibit even higher tendency to excessively form $C_{4-5}$, which are relatively undesired compared to larger hydrocarbons, than $TiO_2$-A-SG (36%, 48%, and ~45% on amorphous $SiO_2$-$Al_2O_3$, Beta, and SSZ-13, respectively), and SSZ-13 also exhibits high selectivity towards undesired $C_3$ (~30%). For zeolites, the enhanced tendency to form $C_{3-5}$ compared to $TiO_2$-A-SG can be rationalized by the shape-selective effects of their microporous structures [39, 42]. The large-pore Beta favors $C_{4-5}$, and small-pore SSZ-13 also favors $C_3$ by increasing the probability for type-B $\beta$-scissions (ones involving one $^2C^+$ and one $^3C^+$, Scheme 2) that have less bulky intermediates than type-A $\beta$-scissions [21]. The more prominent sequential $\beta$-scissions on amorphous $SiO_2$-$Al_2O_3$ than on $TiO_2$-A-SG could be due to stronger polymer adhesion, which will be discussed in detail in the section 3.5. Overall, Figure 6 highlights the superior activity and selectivity of $TiO_2$-A-SG in PP hydrocracking over conventional Brønsted-acidic supports, which is partially attributed to its non-microporous structure.

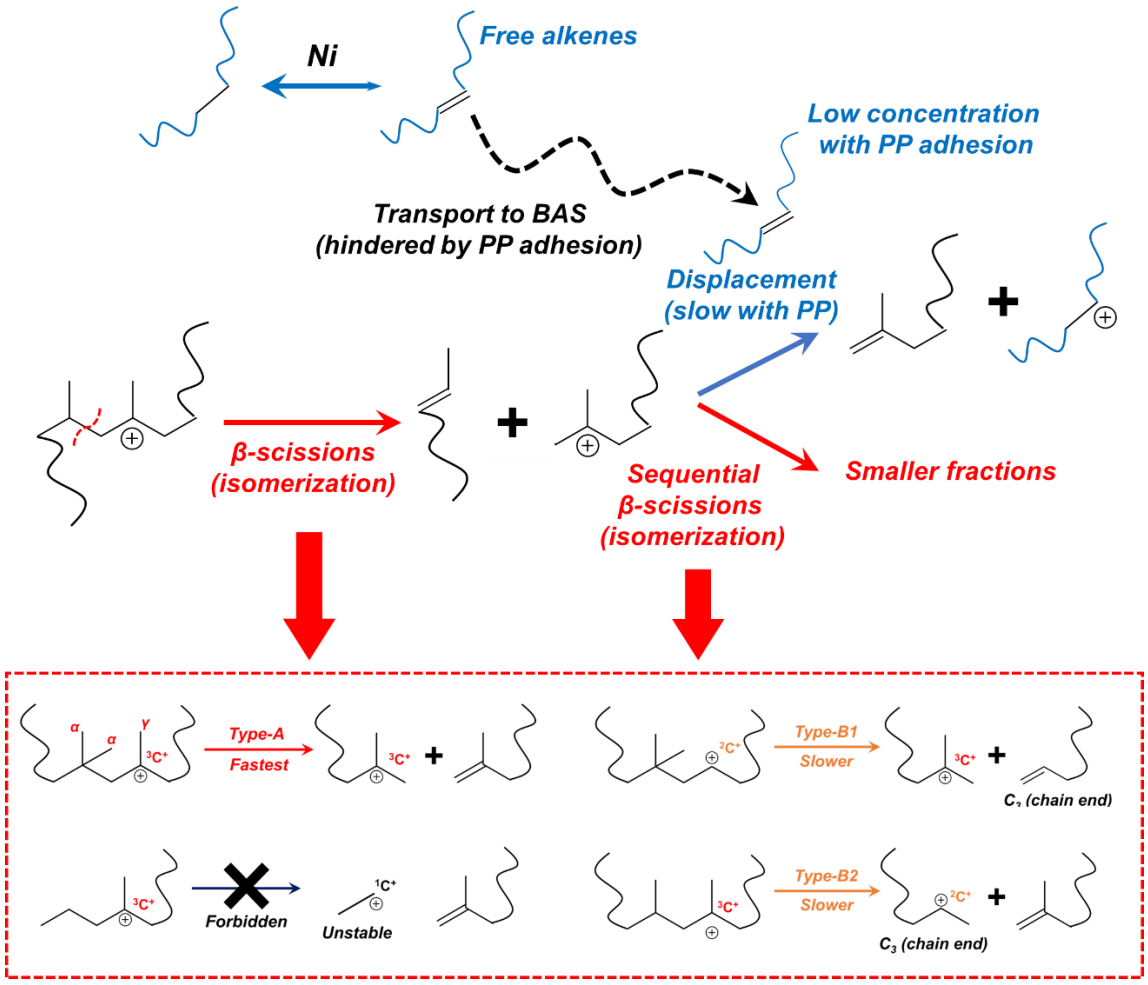


**Scheme 2.** Schematic drawing of possible reaction steps of a carbenium cation ($C^+$) on a BAS in alkane hydrocracking. The blue chains are for labelling molecules other than the adsorbed one. Different types of $\beta$-scissions are shown in the red dashed box.

*3.5 Mechanistic insights on PP hydrocracking over Ni/$TiO_2$-A-SG*

Ni/$TiO_2$-A-SG also offers the opportunity to investigate PP hydrocracking separated from hydrogenolysis. We first varied the Ni loading (coverage). Figure 7a shows that as Ni loading increases, PP conversion increases first at < 0.33 $nm^{-2}$, reaches a plateau between 0.33 and 13 $nm^{-2}$, and then decreases to a negligible level at 27 $nm^{-2}$. The trend indicates that at low Ni loading, the dehydrogenation/hydrogenation steps on Ni are slower than the cracking steps on the BAS, and thus increasing Ni loading facilitates the overall reaction. As Ni loading reaches a certain level,

(de)hydrogenation becomes faster than cracking, resulting in the rate plateau. In addition, 2.6 Pt/$TiO_2$-A-SG also shows the plateau-level rate (17% PP conversion, Figure S7a) despite the significantly better (de)hydrogenation ability of Pt than Ni, further confirming the faster (de)hydrogenation than cracking in the rate-plateau regime. The decrease in activity at very high Ni loading is likely due to the covering of BAS on $TiO_2$-A-SG by Ni, as suggested by the lack of H-bond formation between surface −OH and CO on the sample (Figure S5e).

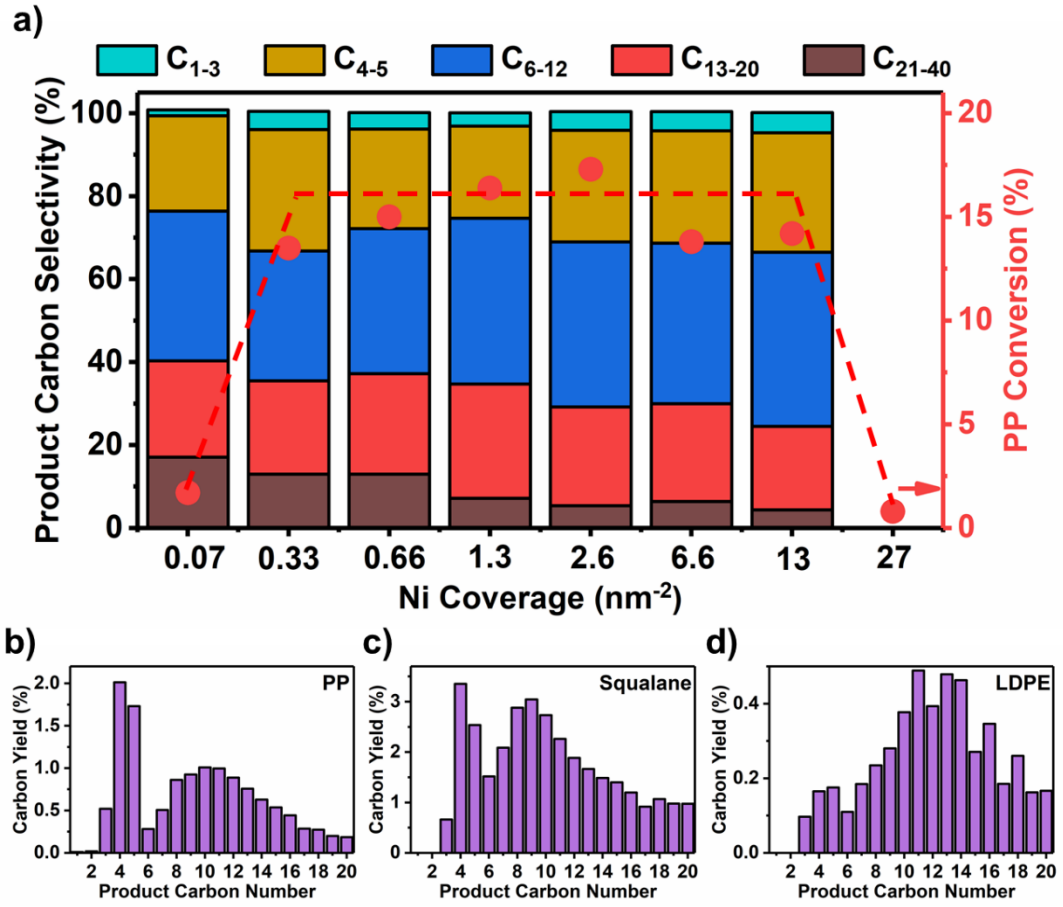


**Figure 7. a)** Effects of Ni coverage on PP hydrocracking over Ni/$TiO_2$-A-SG. Red dots/curves represent the PP conversion (right *y*-axis), while stacked cyan, yellow, blue, red, and brown bars represent the carbon selectivity towrads $C_{1\text{-}3}$, $C_{4\text{-}5}$, $C_{6\text{-}12}$, $C_{13\text{-}20}$, and $C_{21\text{-}40}$ products. From low- to high-coverage, the corresponding Ni wt% on each catalyst is 0.04, 0.25, 0.5, 1, 2, 5, 10, and 20. **b) – d)** The carbon distribution among $C_{1\text{-}20}$ products from the hydrocracking of PP (17% conversion), squalane (50% conversion), and LDPE (9% conversion) respectively, on 2.6 Ni/$TiO_2$-A-SG. Reaction conditions: 260 °C, 30 bar $H_2$, 1 g PP/squalane/LDPE, 30 mg catalyst and 3 h for PP and LDPE, 8 mg and 2 h for squalane.

In terms of product distribution, Figure 7a shows that through the entire Ni loading range, the formation of $C_{1-3}$ is minimal, as expected from $\beta$-scissions, but the high selectivity towards $C_{4-5}$ (> 20%, bar graphs of two representative examples shown in Figures 7b and S7b, respectively) that reflects extensive sequential $\beta$-scissions also persists. In small-alkane hydrocracking, sequential $\beta$-scissions are common on catalysts with weak (de)hydrogenation ability, which causes slow alkane dehydrogenation relative to $\beta$-scissions, and thus low concentration of free alkenes that cannot displace cracked $C^+$ fragments from the BAS effectively [21, 42, 50, 51]. Thus, the high $C_{4-5}$ selectivity is expected on the low-loading 0.07 Ni/$TiO_2$-A-SG. Nonetheless, at higher Ni loading and with 2.6 $nm^{-2}$ Pt (Figure S7a), dehydrogenation is faster than cracking, as the plateaued rate suggests, and thus alkene-alkane equilibrium is reached (referred to as "ideal cracking"). In small-alkane hydrocracking, the equilibrated free-alkene concentration under typical reaction conditions ($T$ = 240 – 300 °C, $P_{H2}$ = 20 – 50 bar) is high enough to avoid extensive sequential $\beta$-scissions [21]. Therefore, the extensive sequential $\beta$-scissions on these catalysts are intriguing. We also tested 6.6 Ni/$TiO_2$-A-SG under lower $P_{H2}$ (5 and 2 bar), to increase the free-alkene concentration at equilibrium, but the high selectivity towards $C_{4-5}$ persisted (Figures S7c-d).

We noticed that compared to PP, both squalane and LDPE show significantly less tendency for $C_{4-5}$ formation (Figures 7c-d compared to Figure 7b, Figures S7e-f compared to Figure S7b at similar conversions). Based on these observations, we propose that the strong tendency of PP to go through sequential $\beta$-scissions is due to the combination of strong polymer adhesion to catalyst surfaces, and fast $\beta$-scissions with abundant $^3C$. The strong adhesion of the polymer can involve multi-point adsorption, with both C=C bonds formed *in situ* and C−C bonds that can adsorb on Ni dehydrogenatively, as well as the strong van der Waals interactions between the long chains and catalyst surfaces. When one polymer molecule adheres to the catalyst, it "shields" the BAS and

prevents free C=C bonds in other molecules to access them, leading to its untimely displacement and thus sequential $\beta$-scissions. We note that the adhered polymer molecule itself could have multiple free C=C bonds, but even if these free C=C can effectively displace cracked $C^+$, the next $\beta$-scissions still occur to the same molecule. Compared to PP, the much smaller squalane molecule has much weaker "shielding effect" on the BAS. On the other hand, due to the strong dependence of the rate of $\beta$-scissions on the branching level of $C^+$ intermediates, the much less branched LDPE allows significantly more time for the displacement of $C^+$ to occur between two $\beta$-scissions. Besides, the lower starting $M_W$ (~4,000 compared to ~250,000) of LDPE used in this work could also reduce the "shielding effect". The proposed explanation resonates with the previous study invoking the strong adhesion of LDPE on Pt/WZr catalysts to rationalize the sequential isomerization at the initial stage [29]. As a side note, in squalane hydrocracking, the conversion is significantly higher on 2.6 than on 0.33 Ni/$TiO_2$-A-SG (50% in Figure 7c, compared to 16% in Figure S7e), indicating that on the latter, (de)hydrogenation is slower than cracking. This is in contrast to the observation in PP hydrocracking, that (de)hydrogenation is faster than cracking between 0.33 and 2.6 $nm^{-2}$ Ni (Figure 7a). The contrast emphasizes that the unique properties of long-chain POs compared to smaller alkanes have significant implications on hydrocracking.

The reaction time was varied on 1.3 Ni/$TiO_2$-A-SG to track the reaction progress. Figure 8a shows that PP conversion is linearly proportional to the reaction time below 100%. The reaction starts in the neat condition, but smaller hydrocarbons produced continuously act as "solvents" for PP. Thus, the independent PP conversion rate with its concentration, resembling "zero-order kinetics" in small-molecule reactions, suggests that even in the presence of smaller hydrocarbons, the catalyst surface is saturated by polymers, as a result of their strong adhesion. Meanwhile, Figure 8b shows that all $C_{31\text{-}40}$ products appear at 3% and accumulate until ~70% PP conversion

with constant selectivity (Figure S8), indicating that they are all primary products with limited secondary reactions. After 100% PP conversion, the > $C_{20}$ products (purple and brown) are cracked into smaller fragments. The lack of secondary reactions at < 100% PP conversion is also explained by the strong polymer adhesion, which prevents the re-adsorption of products. The preferred adsorption of polymers over small alkanes observed here resonates with previous reports on LDPE hydrocracking [29] and PO hydrogenolysis [9]. We note that PP is converted and products are formed in the first 0.5 h (Figure S8a). This is in contrast to the induction period observed in LDPE hydrocracking [29], and can be attributed to the abundance of $^{3}C$ in the virgin PP structure allowing type-B $\beta$-scissions to occur without significant preceding isomerization.

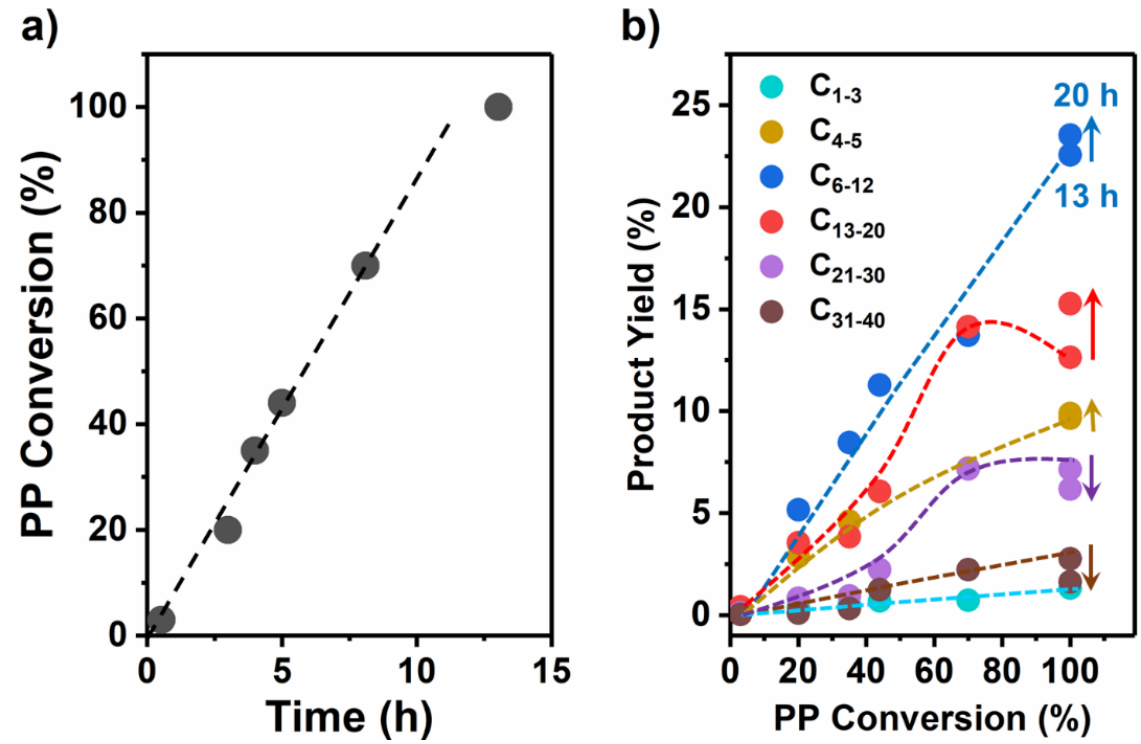


**Figure 8.** Time-dependence of PP hydrocracking over 1.3 Ni/$TiO_2$-A-SG. **a)** Variations in the PP conversion with reaction time. **b)** Variations of the yield of $C_{1\text{-}3}$, $C_{4\text{-}5}$, $C_{6\text{-}12}$, $C_{13\text{-}20}$, and $C_{21\text{-}40}$ products (cyan, yellow, blue, red, and brown dots/curves, respectively) with PP conversion. The two series of data points at 100% PP conversion were measured with 13 and 20 h reaction time, resepctively, and the colored arrows next to them represent the moving direction from 13 to 20 h. Reaction conditions: 260 °C, 30 bar $H_2$, 1 g PP, 30 mg catalyst.

One distinct character of hydrocracking from hydrogenolysis and Haag-Dessau cracking is the fast isomerization of carbenium ions through alkyl/hydride shifts or protonated cyclopropanes [41, 50, 51]. In fact, even at 3% PP conversion, the $C_{10}$ products are highly isomerized (> 60%), indicating that although the isomerization is not required before $\beta$-scissions, it is fast enough on Ni/$TiO_2$-A-SG, so that when PP is cracked into the $C_{10}$ range, it has been highly isomerized. This is expected because the virgin PP structure has no $\alpha$, $\alpha$, $\gamma$-configurations (Scheme 2) to allow the fastest type-A $\beta$-scissions without isomerization [21, 42, 49-51], while studies on small alkanes agreed that the rate of type-B $\beta$-scissions is much slower than that of type-A isomerization (ones not changing branching level) and comparable with that of type-B isomerization (ones increasing or decreasing branching level) [21, 42, 49-51]. The faster isomerization than type-B $\beta$-scissions is further supported by the large amount of isomerized, non-cracked products observed in squalane hydrocracking at low conversion (Figure S9). Furthermore, since $C_3$ are exclusively produced by type-B $\beta$-scissions (Scheme 2), the much lower $C_3$ yield than $C_4$ (Figures 6, S7, and S8) suggests that the type-B isomerization – type-A $\beta$-scission sequence is preferred over type-B $\beta$-scission, in agreement with the observations in small-alkane hydrocracking [21, 29, 42, 49-51].

### *3.6 Practical considerations of PP hydrocracking over Ni/$TiO_2$-A-SG*

In this section we briefly address several aspects associated with using Ni/$TiO_2$-A-SG for PP hydrocracking in practical operations. First, in Figure 8a, the dependence of PP conversion on reaction time closely follows "zero-order kinetics" predicted by the strong PP adhesion. This, along with the fact that in Figure 8b, > $C_{20}$ products are further converted into smaller ones, indicates that Ni/$TiO_2$-A-SG does not deactivate significantly during the reaction. This is expected considering we applied high $P_{H2}$ (30 bar) and a metal with strong hydrogenation ability (Ni) in the experiments to prevent coke formation by the fast hydrogenation of unsaturated products. We note

that for reactions performed in polymer melts in a batch reactor, reliable catalyst recyclability test is challenging to conduct. Used catalyst can only be recovered when all polymers are converted, but performing reactions to 100% conversion automatically invalidates the test. On the other hand, we characterized used 0.66 Ni/$TiO_2$-A-SG catalyst with STEM and EDX mapping, which show relatively uniform Ni nanoparticles of $d = 12 \pm 3$ nm (Figure S10b). Interestingly, the same sample reduced by 30 bar $H_2$ at 260 ℃ mostly has highly dispersed Ni, with only sparse nanoparticles identified (Figure S10a). The contrast suggests that the presence of adhered polymer on catalyst surface could affect the reduction and aggregation behaviors of metal species.

Next, since Cl is a common catalyst poison, we evaluated the effect of low-concentration PVC on PP hydrocracking over Ni/$TiO_2$-A-SG. Table S3 shows that for both 0.66 and 6.6 Ni/$TiO_2$-A-SG, 1% PVC mixed in the feedstock deactivates the catalyst by ~60%, without significantly altering the selectivity. The level of the PVC poisoning effect is similar with hydrogenolysis on Ru/$CeO_2$ [24], and much less severe than hydrogenolysis on Ru/C [9]. Interestingly, Table S3 also shows that 1% PVC allows PP hydrocracking to occur on 0.07 Ni/rutile-$TiO_2$ ($TiO_2$-R), which is inactive for the reaction with pure PP feedstock under the testing conditions. Therefore, PVC might also modify the acidity of $TiO_2$ surfaces and thus enhance their reactivity. Finally, we tested the hydrocracking of two PP-plastic products, a surgical mask, and a laboratory-use vial, on 0.66 Ni/$TiO_2$-A-SG. Table S4 shows that the mask cannot be converted, possibly due to the additives in it poisoning the catalyst, while the vial can be effectively converted with similar selectivity.

*3.7 Comparisons between the two PO hydro-conversion pathways*

Here we briefly discuss the relative advantages of hydrocracking and hydrogenolysis reactions in PO upcycling. Due to the relative stability of $C^+$ , hydrocracking produces trace $C_{1-2}$

and minimal $C_3$ (Scheme 2) [42, 49-51]. In contrast, in hydrogenolysis, the first C−C bond cleavage does not discriminate against $C_{1-3}$, and if the desorption is slow, the sequential C−C cleavage with a terminal C adsorbed strongly favors $C_1$ [68, 69, 72]. In hydrocracking, $H_2$ is only needed for the hydrogenation of cracked unsaturated hydrocarbons, without directly participating in the C−C bond cleavage. As a result, it demands lower $P_{H2}$ than hydrogenolysis. In fact, at $P_{H2}$ = 5 bar, the bifunctional Ru/$TiO_2$-A-SG converts PP much more effectively (223 $g_{PP}$ $g_{Ru}^{-1}$ $h^{-1}$, Figure 4a) than the most active monofunctional catalyst, Ru/$CeO_2$ (~30 $g_{PP}$ $g_{Ru}^{-1}$ $h^{-1}$ [24]). Furthermore, in hydrocracking, the metal only catalyzes (de)hydrogenation, and hence non-noble metals active for hydrogenation, such as Ni, can be used, while only Ru/Rh effectively catalyze PO hydrogenolysis at < 300 ℃ [7, 9]. Finally, the isomerization in hydrocracking leads to higher degree of branching of products from PE than hydrogenolysis. On the other hand, hydrogenolysis might be more effective in converting sparsely branched POs, such as PE, as Table 2 and Figure 5 suggest. In addition, we note that on 0.07 Ru/$TiO_2$-A-SG, when $P_{H2}$ increases from 15 to 45 bar, the overall rate remains similar while the hydrogenolysis rate increases, indicating decreasing hydrocracking rate (Figure 4a). As discussed, at such low Ru loading, the alkane-alkene equilibrium is not established. Under these conditions, hydrogenolysis on Ru consumes the dehydrogenated surface intermediates, reducing the amount of desorbed alkenes (Scheme 1). Therefore, the two pathways compete with each other, and the faster hydrogenolysis at higher $P_{H2}$ leads to lower free-alkene concentration, and hence slower hydrocracking.

## 4. Conclusions

Ru and Ni supported on $TiO_2$-A-SG are efficient catalysts for the hydro-conversion of POs into small alkanes. The BAS on $TiO_2$-A-SG allows hydrocracking, leading to higher catalytic

efficiency, less undesired $C_{1-3}$ products, more high-valued liquid products with narrower distribution and more isomers, than monofunctional Ru hydrogenolysis catalysts, particularly with PP as the substrate. Between the two reaction pathways on Ru/$TiO_2$-A-SG, hydrocracking is more prominent at lower $P_{H2}$, with lower Ru loading, and with more branched substrate, since the abundance of $^3$C allows fast $\beta$-scissions and hinders hydrogenolysis. Non-noble-metal Ni supported on $TiO_2$-A-SG can also catalyze PP hydrocracking, showing better activity and selectivity than conventional Brønsted-acidic supports, particularly zeolites, partially due to its non-microporous structure. Mechanistic studies on Ni/$TiO_2$-A-SG provided evidence for fast isomerization and strong polymer adhesion. The latter hinders the accessibility of active sites to other molecules, which prevents secondary reactions and enhances the tendency for sequential $\beta$-scissions, in turn promoting the production of $C_{4-12}$, particularly $C_{4-5}$. Low-concentration of PVC partially poisons Ni/$TiO_2$-A-SG, but could also modify the acidity of $TiO_2$ and hence enable hydrocracking on rutile. This work presented novel type of metal-BAS bifunctional catalysts that carry significant potentials in PO hydro-conversion, elucidated the contribution of the two distinct reaction pathways, and advanced the mechanistic understanding of PO hydrocracking.

## CRediT authorship contribution statement

Linxiao Chen: Conceptualization; Methodology; Investigation; Writing – Original Draft; Julia D. Moreira: Investigation; Writing – Review & Editing; Laura C. Meyer: Methodology; Investigation; Writing – Review & Editing; Janos Szanyi: Conceptualization; Writing – Review & Editing; Supervision; Project administration; Funding acquisition.

## Declaration of Competing Interest

The authors declare no competing interests for this work.

**Acknowledgement**

This work was supported by the U.S. Department of Energy, Office of Science, Basic Energy Sciences, Chemical Sciences, Geosciences, and Biosciences Division, Catalysis Science program, FWP 47319. PNNL is a multiprogram national laboratory operated for DOE by Battelle. Use of the Stanford Synchrotron Radiation Lightsource, SLAC National Accelerator Laboratory, is supported by the U.S. Department of Energy, Office of Science, Office of Basic Energy Sciences under Contract No. DE-AC02-76SF00515. We acknowledge Dr. Simon R. Bare, Dr. Adam S. Hoffman, Dr. Jiyun Hong, and Dr. Jorge Perez-Aguilar at SLAC for the assistance of XAS measurements. We acknowledge Dr. Libor Kovarik, Dr. Mark E. Bowden, Mr. Mark H. Engelhard, Ms. Shari X. Li, and Dr. Sungmin Kim at PNNL for STEM, XRD, XPS, BET, and pyridine-IR measurements. We acknowledge Dr. Johannes A. Lercher, Dr. Oliver Y. Gutiérrez, Dr. Lillian V. Hale, and Dr. Feng Gao at PNNL for insightful discussions.

## References


[1] D.K.A. Barnes, F. Galgani, R.C. Thompson, M. Barlaz, Accumulation and fragmentation of plastic debris in global environments, Philos. Trans. R. Soc. Lond., B, Biol. Sci., 364 (2009) 1985-1998.
[2] R. Geyer, J.R. Jambeck, K.L. Law, Production, use, and fate of all plastics ever made, Sci. Adv., 3 (2017) e1700782.
[3] L.D. Ellis, N.A. Rorrer, K.P. Sullivan, M. Otto, J.E. McGeehan, Y. Román-Leshkov, N. Wierckx, G.T. Beckham, Chemical and biological catalysis for plastics recycling and upcycling, Nat. Catal., 4 (2021) 539-556.
[4] W. Kaminsky, B. Schlesselmann, C. Simon, Olefins from polyolefins and mixed plastics by pyrolysis, J. Anal. Appl. Pyrolysis, 32 (1995) 19-27.
[5] R. Bagri, P.T. Williams, Catalytic pyrolysis of polyethylene, J. Anal. Appl. Pyrolysis, 63 (2002) 29-41.
[6] W. Kaminsky, I.-J.N. Zorriqueta, Catalytical and thermal pyrolysis of polyolefins, J. Anal. Appl. Pyrolysis, 79 (2007) 368-374.
[7] J.E. Rorrer, C. Troyano-Valls, G.T. Beckham, Y. Román-Leshkov, Hydrogenolysis of Polypropylene and Mixed Polyolefin Plastic Waste over Ru/C to Produce Liquid Alkanes, ACS Sustain. Chem. Eng., 9 (2021) 11661-11666.
[8] P.A. Kots, S. Liu, B.C. Vance, C. Wang, J.D. Sheehan, D.G. Vlachos, Polypropylene Plastic Waste Conversion to Lubricants over Ru/TiO2 Catalysts, ACS Catal., 11 (2021) 8104-8115.
[9] L. Chen, Y. Zhu, L.C. Meyer, L.V. Hale, T.T. Le, A. Karkamkar, J.A. Lercher, O.Y. Gutiérrez, J. Szanyi, Effect of reaction conditions on the hydrogenolysis of polypropylene and polyethylene into gas and liquid alkanes, React. Chem. Eng., 7 (2022) 844-854.
[10] Y. Nakaji, M. Tamura, S. Miyaoka, S. Kumagai, M. Tanji, Y. Nakagawa, T. Yoshioka, K. Tomishige, Low-temperature catalytic upgrading of waste polyolefinic plastics into liquid fuels and waxes, Appl. Catal., B, 285 (2021) 119805.
[11] Y. Jing, Y. Wang, S. Furukawa, J. Xia, C. Sun, M.J. Hülsey, H. Wang, Y. Guo, X. Liu, N. Yan, Towards the Circular Economy: Converting Aromatic Plastic Waste Back to Arenes over a Ru/Nb2O5 Catalyst, Angew. Chem. Int. Ed., 60 (2021) 5527-5535.
[12] F. Zhang, M. Zeng, R.D. Yappert, J. Sun, Y.-H. Lee, A.M. LaPointe, B. Peters, M.M. Abu-Omar, S.L. Scott, Polyethylene upcycling to long-chain alkylaromatics by tandem hydrogenolysis/aromatization, Science, 370 (2020) 437-441.
[13] A. Tennakoon, X. Wu, A.L. Paterson, S. Patnaik, Y. Pei, A.M. LaPointe, S.C. Ammal, R.A. Hackler, A. Heyden, I.I. Slowing, G.W. Coates, M. Delferro, B. Peters, W. Huang, A.D. Sadow, F.A. Perras, Catalytic upcycling of high-density polyethylene via a processive mechanism, Nat. Catal., 3 (2020) 893-901.
[14] S.D. Jaydev, A.J. Martín, J. Pérez-Ramírez, Direct Conversion of Polypropylene into Liquid Hydrocarbons on Carbon-Supported Platinum Catalysts, ChemSusChem, 14 (2021) 5179-5185.
[15] C. Jia, S. Xie, W. Zhang, N.N. Intan, J. Sampath, J. Pfaendtner, H. Lin, Deconstruction of high-density polyethylene into liquid hydrocarbon fuels and lubricants by hydrogenolysis over Ru catalyst, Chem Catalysis, 1 (2021) 437-455.
[16] A.H. Mason, A. Motta, A. Das, Q. Ma, M.J. Bedzyk, Y. Kratish, T.J. Marks, Rapid atom-efficient polyolefin plastics hydrogenolysis mediated by a well-defined single-site electrophilic/cationic organo-zirconium catalyst, Nat. Comm., 13 (2022) 7187.

[17] W.-T. Lee, A. van Muyden, F.D. Bobbink, M.D. Mensi, J.R. Carullo, P.J. Dyson, Mechanistic classification and benchmarking of polyolefin depolymerization over silica-alumina-based catalysts, Nat. Comm., 13 (2022) 4850.
[18] R.A. Hackler, J.V. Lamb, I.L. Peczak, R.M. Kennedy, U. Kanbur, A.M. LaPointe, K.R. Poeppelmeier, A.D. Sadow, M. Delferro, Effect of Macro- and Microstructures on Catalytic Hydrogenolysis of Polyolefins, Macromolecules, 55 (2022) 6801-6810.
[19] M. Tamura, S. Miyaoka, Y. Nakaji, M. Tanji, S. Kumagai, Y. Nakagawa, T. Yoshioka, K. Tomishige, Structure-activity relationship in hydrogenolysis of polyolefins over Ru/support catalysts, Appl. Catal., B, 318 (2022) 121870.
[20] B.C. Vance, P.A. Kots, C. Wang, J.E. Granite, D.G. Vlachos, Ni/SiO2 catalysts for polyolefin deconstruction via the divergent hydrogenolysis mechanism, Appl. Catal., B, 322 (2023) 122138.
[21] J. Weitkamp, Catalytic Hydrocracking—Mechanisms and Versatility of the Process, ChemCatChem, 4 (2012) 292-306.
[22] J. Duan, W. Chen, C. Wang, L. Wang, Z. Liu, X. Yi, W. Fang, H. Wang, H. Wei, S. Xu, Y. Yang, Q. Yang, Z. Bao, Z. Zhang, Q. Ren, H. Zhou, X. Qin, A. Zheng, F.-S. Xiao, Coking-Resistant Polyethylene Upcycling Modulated by Zeolite Micropore Diffusion, J. Am. Chem. Soc., 144 (2022) 14269-14277.
[23] P.A. Kots, B.C. Vance, D.G. Vlachos, Polyolefin plastic waste hydroconversion to fuels, lubricants, and waxes: a comparative study, React. Chem. Eng., 7 (2022) 41-54.
[24] L. Chen, L.C. Meyer, L. Kovarik, D. Meira, X.I. Pereira-Hernandez, H. Shi, K. Khivantsev, O.Y. Gutiérrez, J. Szanyi, Disordered, Sub-Nanometer Ru Structures on CeO2 are Highly Efficient and Selective Catalysts in Polymer Upcycling by Hydrogenolysis, ACS Catal., 12 (2022) 4618-4627.
[25] J.E. Rorrer, G.T. Beckham, Y. Román-Leshkov, Conversion of Polyolefin Waste to Liquid Alkanes with Ru-Based Catalysts under Mild Conditions, JACS Au, 1 (2021) 8-12.
[26] X. Wu, A. Tennakoon, R. Yappert, M. Esveld, M.S. Ferrandon, R.A. Hackler, A.M. LaPointe, A. Heyden, M. Delferro, B. Peters, A.D. Sadow, W. Huang, Size-Controlled Nanoparticles Embedded in a Mesoporous Architecture Leading to Efficient and Selective Hydrogenolysis of Polyolefins, J. Am. Chem. Soc., 144 (2022) 5323-5334.
[27] Y. Nakagawa, S.-i. Oya, D. Kanno, Y. Nakaji, M. Tamura, K. Tomishige, Regioselectivity and Reaction Mechanism of Ru-Catalyzed Hydrogenolysis of Squalane and Model Alkanes, ChemSusChem, 10 (2017) 189-198.
[28] J.E. Rorrer, A.M. Ebrahim, Y. Questell-Santiago, J. Zhu, C. Troyano-Valls, A.S. Asundi, A.E. Brenner, S.R. Bare, C.J. Tassone, G.T. Beckham, Y. Román-Leshkov, Role of Bifunctional Ru/Acid Catalysts in the Selective Hydrocracking of Polyethylene and Polypropylene Waste to Liquid Hydrocarbons, ACS Catal., 12 (2022) 13969-13979.
[29] B.C. Vance, P.A. Kots, C. Wang, Z.R. Hinton, C.M. Quinn, T.H. Epps, L.T.J. Korley, D.G. Vlachos, Single pot catalyst strategy to branched products via adhesive isomerization and hydrocracking of polyethylene over platinum tungstated zirconia, Appl. Catal., B, 299 (2021) 120483.
[30] S. Liu, P.A. Kots, B.C. Vance, A. Danielson, D.G. Vlachos, Plastic waste to fuels by hydrocracking at mild conditions, Sci. Adv., 7 (2021) eabf8283.
[31] B. Du, X. Chen, Y. Ling, T. Niu, W. Guan, J. Meng, H. Hu, C.-W. Tsang, C. Liang, Hydrogenolysis-Isomerization of Waste Polyolefin Plastics to Multibranched Liquid Alkanes, ChemSusChem, n/a e202202035.

[32] G. Zichittella, A.M. Ebrahim, J. Zhu, A.E. Brenner, G. Drake, G.T. Beckham, S.R. Bare, J.E. Rorrer, Y. Román-Leshkov, Hydrogenolysis of Polyethylene and Polypropylene into Propane over Cobalt-Based Catalysts, JACS Au, 2 (2022) 2259-2268.
[33] C. Wang, T. Xie, P.A. Kots, B.C. Vance, K. Yu, P. Kumar, J. Fu, S. Liu, G. Tsilomelekis, E.A. Stach, W. Zheng, D.G. Vlachos, Polyethylene Hydrogenolysis at Mild Conditions over Ruthenium on Tungstated Zirconia, JACS Au, 1 (2021) 1422-1434.
[34] G. Celik, R.M. Kennedy, R.A. Hackler, M. Ferrandon, A. Tennakoon, S. Patnaik, A.M. LaPointe, S.C. Ammal, A. Heyden, F.A. Perras, M. Pruski, S.L. Scott, K.R. Poeppelmeier, A.D. Sadow, M. Delferro, Upcycling Single-Use Polyethylene into High-Quality Liquid Products, ACS Cent. Sci., 5 (2019) 1795-1803.
[35] S.P. Ertem, C.E. Onuoha, H. Wang, M.A. Hillmyer, T.M. Reineke, T.P. Lodge, F.S. Bates, Hydrogenolysis of Linear Low-Density Polyethylene during Heterogeneous Catalytic Hydrogen–Deuterium Exchange, Macromolecules, 53 (2020) 6043-6055.
[36] A.b. Jumah, A.A. Tedstone, A.A. Garforth, Hydrocracking of virgin and post-consumer polymers, Microporous Mesoporous Mater., 315 (2021) 110912.
[37] A. Bin Jumah, V. Anbumuthu, A.A. Tedstone, A.A. Garforth, Catalyzing the Hydrocracking of Low Density Polyethylene, Ind. Eng. Chem. Res., 58 (2019) 20601-20609.
[38] K. Pyra, K.A. Tarach, A. Śrębowata, I. Melián-Cabrera, K. Góra-Marek, Pd-modified beta zeolite for modulated hydro-cracking of low-density polyethylene into a paraffinic-rich hydrocarbon fuel, Appl. Catal., B, 277 (2020) 119070.
[39] N.D. Hesse, R.L. White, Polyethylene catalytic hydrocracking by PtHZSM-5, PtHY, and PtHMCM-41, J. Appl. Polym. Sci., 92 (2004) 1293-1301.
[40] D. Munir, M.F. Irfan, M.R. Usman, Hydrocracking of virgin and waste plastics: A detailed review, Renew. Sust. Energ. Rev., 90 (2018) 490-515.
[41] W. Ding, J. Liang, L.L. Anderson, Hydrocracking and Hydroisomerization of High-Density Polyethylene and Waste Plastic over Zeolite and Silica−Alumina-Supported Ni and Ni−Mo Sulfides, Energy Fuels, 11 (1997) 1219-1224.
[42] T.L.M. Maesen, S. Calero, M. Schenk, B. Smit, Alkane hydrocracking: shape selectivity or kinetics?, J. Catal., 221 (2004) 241-251.
[43] T. Xie, G.R. Wittreich, D.G. Vlachos, Multiscale modeling of hydrogenolysis of ethane and propane on Ru(0001): Implications for plastics recycling, Appl. Catal., B, 316 (2022) 121597.
[44] Y. Cui, Y. Wang, D. Mei, E.D. Walter, N.M. Washton, J.D. Holladay, Y. Wang, J. Szanyi, C.H.F. Peden, F. Gao, Revisiting effects of alkali metal and alkaline earth co-cation additives to Cu/SSZ-13 selective catalytic reduction catalysts, J. Catal., 378 (2019) 363-375.
[45] C. Leyva-Porras, A. Toxqui-Teran, O. Vega-Becerra, M. Miki-Yoshida, M. Rojas-Villalobos, M. García-Guaderrama, J.A. Aguilar-Martínez, Low-temperature synthesis and characterization of anatase TiO2 nanoparticles by an acid assisted sol–gel method, J. Alloys Compd., 647 (2015) 627-636.
[46] L. Chen, L. Kovarik, D. Meira, J. Szanyi, Differentiating and Understanding the Effects of Bulk and Surface Mo Doping on CO2 Hydrogenation over Pd/Anatase-TiO2, ACS Catal., 12 (2022) 13492-13500.
[47] A.S. Hoffman, J.A. Singh, S.F. Bent, S.R. Bare, In situ observation of phase changes of a silica-supported cobalt catalyst for the Fischer-Tropsch process by the development of a synchrotron-compatible in situ/operando powder X-ray diffraction cell, J. Synchrotron Rad., 25 (2018) 1673-1682.

[48] A. Jentys, Estimation of mean size and shape of small metal particles by EXAFS, Phys. Chem. Chem. Phys., 1 (1999) 4059-4063.
[49] J.A. Martens, P.A. Jacobs, J. Weitkamp, Attempts to rationalize the distribution of hydrocracked products. I qualitative description of the primary hydrocracking modes of long chain paraffins in open zeolites, Appl. Catal., 20 (1986) 239-281.
[50] F. Alvarez, F.R. Ribeiro, G. Perot, C. Thomazeau, M. Guisnet, Hydroisomerization and Hydrocracking of Alkanes: 7. Influence of the Balance between Acid and Hydrogenating Functions on the Transformation ofn-Decane on PtHY Catalysts, J. Catal., 162 (1996) 179-189.
[51] M. Steijns, G.F. Froment, Hydroisomerization and hydrocracking. 3. Kinetic analysis of rate data for n-decane and n-dodecane, Ind. Eng. Chem. Prod. Rd., 20 (1981) 660-668.
[52] S. Kotrel, H. Knözinger, B.C. Gates, The Haag–Dessau mechanism of protolytic cracking of alkanes, Microporous Mesoporous Mater., 35-36 (2000) 11-20.
[53] W.O. Haag, R.M. Dessau, R.M. Lago, Kinetics and Mechanism of Paraffin Cracking with Zeolite Catalysts, in: T. lnui, S. Namba, T. Tatsumi (Eds.) Stud. Surf. Sci. Catal., Elsevier1991, pp. 255-265.
[54] A. Corma, A.V. Orchillés, Current views on the mechanism of catalytic cracking, Microporous Mesoporous Mater., 35-36 (2000) 21-30.
[55] F. Lin, Y. Chen, L. Zhang, D. Mei, L. Kovarik, B. Sudduth, H. Wang, F. Gao, Y. Wang, Single-Facet Dominant Anatase TiO2 (101) and (001) Model Catalysts to Elucidate the Active Sites for Alkanol Dehydration, ACS Catal., 10 (2020) 4268-4279.
[56] A.R. Gandhe, S.P. Naik, S.B. Kakodkar, J.B. Fernandes, A highly active anatase TiO2 catalyst for alkylation of phenol with methanol, Catal. Commun., 7 (2006) 285-288.
[57] G. Busca, H. Saussey, O. Saur, J.C. Lavalley, V. Lorenzelli, FT-IR characterization of the surface acidity of different titanium dioxide anatase preparations, Appl. Catal., 14 (1985) 245-260.
[58] K. Hadjiivanov, J. Lamotte, J.-C. Lavalley, FTIR Study of Low-Temperature CO Adsorption on Pure and Ammonia-Precovered TiO2 (Anatase), Langmuir, 13 (1997) 3374-3381.
[59] K.I. Hadjiivanov, D.G. Klissurski, Surface chemistry of titania (anatase) and titania-supported catalysts, Chem. Soc. Rev., 25 (1996) 61-69.
[60] C.O. Areán, A.A. Tsyganenko, O.V. Manoilova, G.T. Palomino, M.P. Mentruit, E. Garrone, Amphipathic hydrogen bonding of CO in protonic zeolites, Chem. Comm., (2001) 455-456.
[61] H. Miyata, Y. Nakagawa, T. Ono, Y. Kubokawa, Infrared studies of acid–base properties of vanadium–titanium oxide and oxidation of alcohols on it, J. Chem. Soc., Faraday Trans.1, 79 (1983) 2343-2353.
[62] C. Martín, G. Solana, V. Rives, G. Marcì, L. Palmisano, A. Sclafani, Physico-chemical properties of WO3/TiO2 systems employed for 4-nitrophenol photodegradation in aqueous medium, Catal. Lett., 49 (1997) 235-243.
[63] L. Chen, L. Kovarik, J. Szanyi, Temperature-Dependent Communication between Pt/Al2O3 Catalysts and Anatase TiO2 Dilutant: the Effects of Metal Migration and Carbon Transfer on the Reverse Water–Gas Shift Reaction, ACS Catal., 11 (2021) 12058-12067.
[64] C. Wang, K. Yu, B. Sheludko, T. Xie, P.A. Kots, B.C. Vance, P. Kumar, E.A. Stach, W. Zheng, D.G. Vlachos, A general strategy and a consolidated mechanism for low-methane hydrogenolysis of polyethylene over ruthenium, Appl. Catal., B, 319 (2022) 121899.
[65] Z. Zhou, S. Pesek, J. Klosin, M.S. Rosen, S. Mukhopadhyay, R. Cong, D. Baugh, B. Winniford, H. Brown, K. Xu, Long Chain Branching Detection and Quantification in LDPE with

Special Solvents, Polarization Transfer Techniques, and Inverse Gated 13C NMR Spectroscopy, Macromolecules, 51 (2018) 8443-8454.
[66] D.W. Flaherty, E. Iglesia, Transition-State Enthalpy and Entropy Effects on Reactivity and Selectivity in Hydrogenolysis of n-Alkanes, J. Am. Chem. Soc., 135 (2013) 18586-18599.
[67] D.W. Flaherty, D.D. Hibbitts, E. Iglesia, Metal-Catalyzed C–C Bond Cleavage in Alkanes: Effects of Methyl Substitution on Transition-State Structures and Stability, J. Am. Chem. Soc., 136 (2014) 9664-9676.
[68] B. Coq, F. Figueras, Structure–activity relationships in catalysis by metals: some aspects of particle size, bimetallic and supports effects, Coord. Chem. Rev., 178-180 (1998) 1753-1783.
[69] B. Coq, F. Figueras, Influence of the hydrocarbon structure on the hydrogenolysis of alkanes over rhodium/alumina catalysts, J. Mol. Catal., 40 (1987) 93-112.
[70] H. Zhou, L. Chen, Y. Guo, X. Liu, X.-P. Wu, X.-Q. Gong, Y. Wang, Hydrogenolysis Cleavage of the Csp2–Csp3 Bond over a Metal-Free NbOPO4 Catalyst, ACS Catal., 12 (2022) 4806-4812.
[71] L. Dong, L. Lin, X. Han, X. Si, X. Liu, Y. Guo, F. Lu, S. Rudić, S.F. Parker, S. Yang, Y. Wang, Breaking the Limit of Lignin Monomer Production via Cleavage of Interunit Carbon–Carbon Linkages, Chem, 5 (2019) 1521-1536.
[72] B. Coq, A. Bittar, R. Dutartre, F. Figueras, Influence of the precursor and the support on the catalytic properties of ruthenium for alkane hydrogenolysis, Appl. Catal., 60 (1990) 33-46.